PHYSICAL REVIEW E **109**, 045301 (2024)

Hybrid lattice-Boltzmann–finite-difference approach for the simulation of micro-phase-change-material slurry in convective flow

Anas Ghannam, Eiyad Abu-Nada,[*] and Anas Alazzam[†]
Mechanical Engineering Department, Khalifa University of Science and Technology, Abu Dhabi 127788, United Arab Emirates

(Received 10 November 2023; accepted 14 March 2024; published 5 April 2024)

In this paper, we present a hybrid numerical scheme that couples the lattice Boltzmann method (LBM) with the finite difference method (FDM) to model micro-phase-change-material (MPCM) suspensions in a minichannel. Within this framework, the LBM was employed to solve the continuity, momentum, and energy equations for the fluid domain, while a Lagrangian scheme replicates the motion of MPCM particles. The LBM is coupled with an FDM solver which operates under the lumped capacitance assumption to address the phase-change phenomena within the microparticles. This hybrid coupling eliminates the necessity for any specific treatment in handling phase transitions and tracking phase interfaces. The proposed method is first evaluated on classic particle cases, demonstrating its ability to achieve four-way coupling. Furthermore, the current model effectively adapted viscosity changes when integrating the microparticles, obviating the need for homogenous viscosity models. Subsequently, the potential of this approach is demonstrated by examining the influence of the near-wall thermal interaction of MPCM particles considering three scenarios based on particle density: light ($\rho_p < \rho_f$), neutrally buoyant ($\rho_p \approx \rho_f$), and dense ($\rho_p > \rho_f$) microparticles. The hybrid approach further revealed insights into the impact of the volume fraction on the heat transfer coefficient as well as on the overall heat transfer coefficient and performance index from a Lagrangian perspective.

DOI: 10.1103/PhysRevE.109.045301

I. INTRODUCTION

Effective heat management is a critical consideration in a wide range of energy conversion applications. Specifically, in electrical devices, the generation of heat is not only undesirable but can also lead to performance inefficiencies and potential damage, as highlighted in the literature [1–3]. To eliminate such undesirable setbacks, various cooling schemes [4–8] were investigated, focusing on enhancing their thermal performance. Conversely, it is imperative to recognize that, while thermal energy reduction proves detrimental in certain applications, it assumes critical significance in others, promising enhanced productivity and efficiency [9]. The common thread weaving through these diverse applications centers on the pivotal role of enhancing heat transfer mechanisms to attain optimal performance.

In pursuit of this objective, the literature has primarily focused on methods that involve multiphase implementations that operate on the principle of absorbing huge amounts of energy during phase transition without any temperature elevation. A material utilizing such physics is called a phase-change material (PCM), offering an intriguing avenue for heat management through its superior thermophysical properties of high-energy storage density and high fusion enthalpy [10]. Nonetheless, PCMs have the drawbacks of leakage problems during the solid-liquid phase transition and low thermal conductivity. To address these limitations, researchers tend to divide the PCM into smaller particles because a PCM at a large scale exhibits uneven temperature distribution within the domain which causes the issue of irregular melting and solidification. Therefore, the suspension of a micro-phase-change material (MPCM) into a carrier fluid to create a heat transfer fluid (HTF) is introduced.

While few studies [11,12] have tested the integration of MPCM in heating channels, the actual physics behind particle mixing has not been extensively represented. The behavior and the physics of solid MPCM particle motion and interactions are not studied significantly. Hence, it is imperative to address this issue by introducing the concept of particle coupling. Notably, existing literature predominantly employs three types of particle coupling: one-way coupling, in which only the fluid influences the solid particle phase; two-way coupling, where both fluid and solid phases exert mutual influence; and four-way coupling, which encompasses the aforementioned effects, interparticle interactions, and particle-wall collisions [13]. The utilization of four-way coupling within the current model permits us to precisely replicate the true behavior of MPCM particles within a fluid flow, thereby enhancing the fidelity of the simulation.

To accomplish this coupling, in this paper, we utilize a simulation approach called the lattice Boltzmann method (LBM). The adoption of the LBM in the realm of multiphase flow has gained notable attention due to its various advantages [14]. The LBM emerged as a computational approach based on the Boltzmann equation, primarily for simulating fluid dynamics. In current research, various multiphase LBM models have been developed. These include the color-gradient [15], free-energy [16], and pseudopotential LBMs [17], among others.

---

[*] eiyad.abunada@ku.ac.ae
[†] anas.alazzam@ku.ac.ae

2470-0045/2024/109(4)/045301(21)

Building on the LBM, the discrete Boltzmann method (DBM) excels in capturing the degrees of nonequilibrium systems, specifically focusing on hydrodynamic and thermodynamic deviations from equilibrium [18]. The LBM is constrained by hydrodynamic equation limitations and is often based on simplifying assumptions about equilibrium and continuity. The DBM, however, is more flexible and accounts for discrete formats [19]. The DBM is particularly proficient at addressing nonequilibrium statistical physics challenges, offering ways to describe nonequilibrium states and effects [20]. The DBM is also popular for understanding the dynamics of multicomponent flow coupled with the tracer particle method. The tracer particle method extends the understanding of complex fluid dynamics and the interaction of different phases, especially in problems such as Rayleigh-Taylor instability (RTI) [21,22] and shock-wave interactions with bubbles [23]. While the DBM offers notable advantages in modeling nonequilibrium systems, in this paper, we employ the standard LBM to model solid-liquid interactions. The reader is referred to a very recent article for comprehensive insights into the DBM [19].

In addressing particle-fluid interactions, specific methods within the LBM have been developed. In the current lattice Boltzmann works of simulating particle suspensions, many lattice Boltzmann models were developed to handle the interaction of the fluid phase and the solid phase. The most common ones are the immersed boundary method (IBM) [24] and the homogenized LBM (HLBM) [25]. The main difference between the HLBM and the IBM is how they represent the particle. The IBM employs Lagrange points but requires interpolation, unlike the HLBM, for the reason that the particle settles on the grid of the fluid. The solid particles in the HLBM are defined as moving porous objects for a smooth shift from the fluid domain to the solid domain [26]. Recently, the HLBM has received attention for the simulation of particles in a flow. Krause *et al.* [26] further extended the model, coupling it with a smoothing parameter based on the local porosity model to enable a smooth transition between the fluid medium and the particle for the purpose of eliminating pressure variations. A three dimensional model with arbitrary shape particles are studied using OpenLB [27].

In the literature, the effectiveness of the HLBM in dealing with the hydrodynamic behavior of particle interaction has been proven. Nevertheless, to deal with the PCM behavior inside a particle, a certain treatment is required either by introducing an LBM that handles such a task or combining the LBM with a secondary numerical method. The preference of the latter solution is solely due to avoiding any additional computational power when dealing with the phase-change interface within the particles which is an additional computationally demanding task. One highly suitable candidate is the finite difference method (FDM) due to its simplicity and efficiency in handling differential equations. It is common in the literature to combine the LBM with the FDM to deal with certain problems of the simulation. For example, Gupta *et al.* [28] utilized the hybrid method in their study by allowing the FDM to deal with polymer dynamics and the LBM to handle the multicomponent viscoelastic flow. Others such as Hosseini *et al.* [29] utilized the FDM to deal with the energy and species field, leaving the flow field to be dealt with by the LBM in the simulation of reacting flow. In the current application, using the lumped capacitance method (LCM) for miniature particles, handling the mushy zone of the solid-liquid interface using specific treatments is no longer needed. The particle is considered to have a single, uniform temperature and melting fraction. The phase change within the particle is handled using the FDM by solving the differential equation proposed by Beasley and Ramanarayanan [30]. The obtained temperature is then coupled to the thermal lattice Boltzmann equation. With an adequate amount of accuracy, the LBM-FDM has a high potential to be robust and efficient in the handling of MPCM particles in a convective flow.

Therefore, in this paper, we demonstrate an approach of coupling the LBM (OpenLB [27]) with our own FDM scheme for handling MPCM particles in a minichannel flow from a Lagrangian discrete perspective. We first discuss the methods and models utilized in this paper. Next, we achieve the complete four-way coupling through the validation of the following tests: single-particle suspension analysis, classic drafting-kissing-tumbling (DKT) investigation, and particle-wall interaction experiment tested by two models. Moving to the thermal aspect of this paper, the particle temperature variation is examined to ensure precise thermal behavior. Since we target the performance of the particles in a forced convective flow in this paper, the velocity profile and thermal behavior of the heated minichannel are validated. Subsequently, we conduct the mesh sensitivity analysis. The viscosity of the slurry is estimated through the sedimentation of a foreign particle within an enclosure filled with the slurry. The results and discussion section is structured to first address three distinct cases of MPCM particles with varying density conditions. The second part of the result section investigates the impact of the MPCM particles on the heat transfer coefficient at the entrance and the developed region of the channel. The analysis is extended to examine the influence of the volume fraction (0.1, 0.2, 0.4, and 0.8%) on the average Nusselt number, friction factor, and performance index (PI) for various flow regimes. Lastly, we conclude this paper with some final remarks.

II. NUMERICAL METHOD

The Navier-Stokes equations (NSEs) that govern the transport of a continuum fluid are expressed as follows:

$$\nabla \cdot \mathbf{u_f} = 0, \tag{1}$$

$$\frac{\partial(\mathbf{u_f})}{\partial t} + \nabla \cdot (\mathbf{u_f}\mathbf{u_f}) = -\frac{1}{\rho_f}\nabla p + \nu(\nabla^2 \mathbf{u_f}) + \mathbf{F_f}, \tag{2}$$

$$\rho_f C_{p_f}\left[\frac{\partial T}{\partial t} + (\mathbf{u_f}\cdot\nabla)\mathrm{T}\right] = \nabla \cdot (k_f\ \nabla \mathrm{T}), \tag{3}$$

where $\mathbf{u_f}$ is the fluid velocity, p is the pressure, $\mathbf{F_f}$ is the total external forces acting on the fluid, k_f is the thermal conductivity of the fluid, C_{p_f} is the specific heat capacity of the fluid. The lattice Boltzmann equation encapsulates this system of equations and can be retracted to the above form using the Chapman-Enskog expansion [31]. The nonlinearity of the NSEs shown on the left-hand side of Eq. (2) and the discontinuities it provides at very small-scale simulations reorient our attention to the LBM where such setbacks are absent.

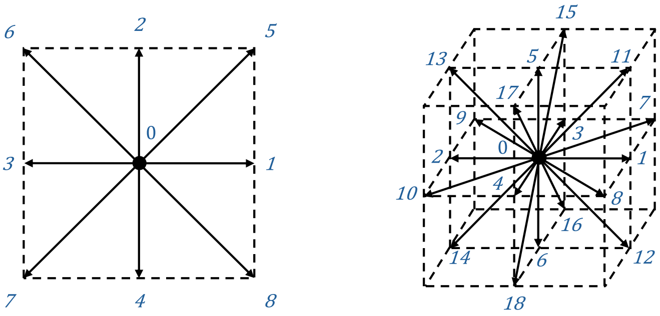

(a) (b)

FIG. 1. (a) $D2Q9$ and (b) $D3Q19$ models.

A. Conventional LBM

In the fundamental LBM method, the Boltzmann transport equation is written as

$$\frac{\partial f}{\partial t} + \mathbf{c} \cdot \nabla f = \Omega. \tag{4}$$

The above equation is discretized into a distribution of fluid particles that stream and collide at a given space and time domain. For an incompressible fluid flow, the Boltzmann equation is described using the density distribution function f_i given as

$$f_i(x + \mathbf{c_i}\Delta t,\ t + \Delta t) = f_i(x,\ t) + \Omega_i(x, t) + S_i, \tag{5}$$

where $\mathbf{c_i}$ is the discrete velocity in the direction of i, and S_i is a source term. The left-hand side of Eq. (5) handles the streaming of the fictitious particles from one node to another, and the right-hand side handles the collision step by a collision operator Ω_i. The most popular approach to approximate the fictitious particle collision is by using the Bhatnagar-Gross-Krook (BGK) model [32], which is known as the single-relaxation-time operator defined as

$$\Omega_i(x, t) = \frac{\Delta t}{\tau_f}\left[f_i^{\mathrm{eq}}(\rho_f, \mathbf{u}) - f_i(x,\ t)\right], \tag{6}$$

where τ_f is the fluid relaxation time coefficient and f_i^{eq} is the equilibrium distribution function specified by

$$f_i^{\mathrm{eq}} = w_i\rho_f\left[1 + \frac{\mathbf{u}\cdot\mathbf{c_i}}{{c_s}^2} + \frac{(\mathbf{u}\cdot\mathbf{c_i})^2}{2{c_s}^4} - \frac{\mathbf{u}\cdot\mathbf{u}}{2{c_s}^2}\right], \tag{7}$$

with

$$\tau_f = \frac{\nu}{{c_s}^2} + 0.5\Delta t, \tag{8}$$

where w_i, ν, and c_s are the weight coefficient, kinematic viscosity, and the lattice speed of sound, respectively. The selection of the velocity model ($D\#Q\#$) establishes the weight coefficients and discrete velocities. The most common velocity models for two- and three-dimensional problems are the $D2Q9$ and $D3Q19$ models (Fig. 1), where D represents the space dimension and Q is the number of possible streaming directions. Therefore, the discrete velocity and weight coefficients for a $D2Q9$ model are [33]

$$\mathbf{c_i} = \begin{cases} (0, 0), & i = 0, \\ c(\pm 1,\ 0),\quad c(0,\ \pm 1), & i = 1, 2, 3, 4, \\ c(\pm 1,\ \pm 1), & i = 5, 6, 7, 8, \end{cases} \tag{9}$$

$$w_i = \begin{cases} \frac{4}{9} & i = 0, \\ \frac{1}{9} & i = 1, 2, 3, 4, \\ \frac{1}{36} & i = 5, 6, 7, 8, \end{cases} \tag{10}$$

and for $D3Q19$ [33]:

$$\mathbf{c}_i = \begin{cases} (0,\ 0,\ 0), & i = 0, \\ c(\pm 1,\ 0,\ 0),\ c(0,\ \pm 1,\ 0),\ c(0,\ 0,\ \pm 1), & i = 1\text{--}6, \\ c(\pm 1,\ \pm 1,\ 0),\ c(\pm 1,\ 0,\ \pm 1),\ c(0,\ \pm 1,\ \pm 1), & i = 7\text{--}18, \end{cases} \tag{11}$$

$$w_i = \begin{cases} \frac{1}{3} & i = 0, \\ \frac{1}{18} & i = 1\text{--}6, \\ \frac{1}{36} & i = 7\text{--}18. \end{cases} \tag{12}$$

Using the above equations, the macroscopic density, pressure, and momentum are calculated from the below equations [33]:

$$\rho_f(x, t) = \sum_{i=0}^{Q-1} f_i(x, t), \tag{13}$$

$$p = \sum_{i=0}^{Q-1} {c_s}^2 f_i(x, t), \tag{14}$$

$$\mathbf{u_f}(x, t) = \frac{1}{\rho_f}\sum_{i=0}^{Q-1} \mathbf{c_i} f_i(x, t). \tag{15}$$

B. HLBM

To account for the presence of the particles in a base fluid, the convectional lattice Boltzmann equation is modified into the homogenized lattice Boltzmann equation. Mainly, the MPCM particle dynamics and behavior are treated in a Lagrangian matter to track their locations and momenta in the flow field and are represented by Newton's second law of motion as

$$m_p \frac{\partial(\mathbf{u_p})}{\partial t} = \mathbf{F_p}, \tag{16}$$

$$J_p \frac{\partial(\omega_\mathbf{p})}{\partial t} = I_p, \tag{17}$$

with m_p, $\mathbf{u_p}$, J_p, $\omega_\mathbf{p}$, $\mathbf{F_p}$, and I_p denoted as the mass of the particle, the velocity of the particle, the moment of inertia, the angular velocity of the particle, the external forces acting on the particle, and the torque acting on the particle. The external forces acting on the particle are mainly gravitational forces, buoyancy forces, and hydrodynamic forces. To smoothen the transition between the particle and the fluid, a velocity mapping function $d_B(x,t)$ ranging from 0 to 1 is used to distinguish between the fluid field and the solid particles. The function $d_B(x,t)$ having a value of 0 corresponds to the fluid domain, where the BGK collision model can be retrieved, and a value of 1 indicates the solid domain. Therefore, the velocity function for such an approach is identified as [26]

$$\bar{\mathbf{u}}(x,t) = \mathbf{u}(x,t) + d_B(x,t)[\mathbf{u_p}(x,t) - \mathbf{u}(x,t)]. \tag{18}$$

The obtained value from the function is implemented in the equilibrium distribution equation [Eq. (7)] of the fluid flow. When the mapping function d_B is equal to 1, the momentum change is fully transferred to the particle for momentum conservation, and the convex function $\bar{u} = u_p$ is not interpreted in Eq. (7). The implementation of the forcing scheme in the LBM needs careful selection, as it affects the accuracy of the method. Thus, different forcing schemes have emerged for higher stability and accuracy. The forcing schemes are incorporated by either adding a source term or altering the macroscopic velocity in the discretized Boltzmann distribution function. Trunk *et al.* [34] tested three forcing schemes and compared their accuracy with one another. The tested forcing schemes are that of Shan and Chen [35], Guo *et al.* [36], and the exact difference method developed by Kupershtokh *et al.* [37]. In this paper, the exact difference forcing scheme was utilized by implementing a source term S_i to Eq. (5) as

$$S_i = f_i^{\text{eq}}(\rho, \mathbf{u} + \mathbf{\Delta u}) - f_i^{\text{eq}}(\rho, \mathbf{u}), \tag{19}$$

with $\mathbf{\Delta u}$ defined as the velocity difference calculated by $\mathbf{\Delta u} = \delta t \frac{\mathbf{F}}{\rho}$, where δt is equal to unity in lattice units.

C. Thermal LBM

To solve the thermal domain, it becomes imperative to incorporate an additional distribution function that effectively characterizes the temperature variations at every individual grid point. Hence, the distribution function for the thermal lattice Boltzmann model proposed by Huang *et al.* [38] is utilized to determine the local temperature using a single relaxation collision scheme. The distribution function g_i is described as

$$g_i(x + \mathbf{c_i}\Delta t,\ t + \Delta t) = g_i(x,\ t) - \frac{\Delta t}{\tau_g}\left[g_i(x,\ t) - g_i^{\text{eq}}(x,\ t)\right], \tag{20}$$

where g_i^{eq} is the thermal equilibrium distribution function, and τ_g is the thermal relaxation time given as

$$\tau_g = \frac{\alpha_f}{{c_s}^2} + 0.5\Delta t, \tag{21}$$

in which α is the thermal diffusivity. The common discrete velocity set selected for the thermal distribution function is $D2Q5$ and is considered sufficient and stable for this paper [39–42]. The equilibrium distribution function responsible for the relaxation of the fictitious particles is obtained from

$$g_i^{\text{eq}} = w_i T\left(1 + \frac{\mathbf{u}\cdot\mathbf{c_i}}{{c_s}^2}\right). \tag{22}$$

To obtain the macroscopic temperature, the zeroth moment of the thermal distribution function is used to express the temperature as

$$T = \sum_{i=0}^{Q-1} g_i(x,t). \tag{23}$$

D. Hybrid lattice Boltzmann with finite difference approach

The next stage of this paper is to establish the thermal coupling between the fluid and the particle in the thermal domain. With a Biot number < 1 for small particles, a lumped capacitance approach is adopted. The instantaneous uniform temperature of the solid particle is attained from the energy equation as [43]

$$\frac{dT_p}{dt} = \xi(T_f - T_p), \tag{24}$$

where ξ is the thermal constant obtained from

$$\xi = \frac{6k_f Nu_p}{\rho_p C_p {D_p}^2}. \tag{25}$$

The instantaneous uniform particle temperature $T_p(t)$ is then coupled on the LBM grid overlapping with that of the particle. The subscript p represents the properties of the particle such as the Nusselt number, density, specific heat capacity, and diameter. The Nusselt number of a particle (Nu_p) describes the ratio of convective heat transfer to conduction heat transfer within the fluid across the surface of the particle.

To model the thermal aspect of phase change inside the particle, the Beasley and Ramanarayanan [30] model was introduced:

$$\frac{dT_p}{dt} = \begin{cases} \frac{6U_p(T_f - T_{\text{PCM}})}{\rho_{p,ss}C_{p,ss}D_p}, & \text{when } \gamma = 0, \\ \frac{6U_p(T_f - T_{\text{PCM}})}{\rho_{p,ls}C_{p,ls}D_p}, & \text{when } \gamma = 1, \\ \frac{6U_p(T_f - T_{\text{PCM}})}{\rho_{p,\text{mushy}}C_{p,\text{mushy}}D_p}, & \text{when } 0 < \gamma < 1. \end{cases} \tag{26}$$

Here, the subscripts ss, ls, and mushy represent the property at solidus temperature, at liquidus temperature, and in between both states, respectively. The advantage of using this approach enables the accurate prediction of temporal temperature variation during phase transition. Such a temperature rise is described as phase trajectory. The model depends on the mushy specific heat capacity C_{mushy}, mushy density ρ_{mushy}, and liquid fraction γ, which are obtained based on the PCM properties from [44]

$$C_{\text{mushy}} = \frac{H_L}{\Delta T_{\text{Melting}}}, \tag{27}$$

$$\rho_{\text{mushy}} = \gamma \rho_{p,ls} + (1-\gamma)\rho_{p,ss}, \tag{28}$$

$$\gamma = \frac{(T_p - T_{\text{Melting,start}})}{\Delta T_{\text{Melting}}}, \tag{29}$$

where H_L is the latent heat of melting, and $\Delta T_{\text{Melting}}$ is the difference between saturation temperatures. To obtain the convective heat transfer coefficient U_p, the Nusselt number of the particle Nu_p is approximated using the empirical correlation for small spherical particles of Ranz and Marshall [45] as

$$\text{Nu}_p = 2 + 0.6(\text{Pr})^{1/3}(\text{Re}_p)^{1/2}. \tag{30}$$

Here, Re_p is the relative particle's Reynolds number defined by

$$\text{Re}_p = \frac{D_p|\mathbf{u_f} - \mathbf{u_p}|}{\nu}. \tag{31}$$

The empirical equation [Eq. (30)] is valid for the laminar region specifically when the Reynolds number is below the limit of 10^4 [46], which is suitable for this paper. Even with the lack of updated correlations, Eq. (30) is adopted extensively in the literature on micro/nanoparticles and is deemed to project adequate estimation of the convective coefficient. By applying the first-order forward FDM on either Eq. (24) or (26), the differential equation is discretized into

$$\frac{dT_p}{dt} = \frac{T_p^{k+1} - T_p^k}{\Delta t} + O(\Delta t), \tag{32}$$

where Δt is the time step, and $O(\Delta t)$ is the order of accuracy. As shown in Eq. (32), the order of accuracy is substantially low. Thereby, for a more stable and accurate model, a backward difference model with second-order accuracy is used:

$$\frac{dT_p}{dt} = \frac{3T_p^k - 4T_p^{k-1} + T_p^{k-2}}{2\Delta t} + O(\Delta t^2). \tag{33}$$

Here, the difference scheme solves temperature information for k using the values obtained from the previous time steps. The current algorithm of the hybrid numerical method is illustrated in Fig. 2. Two loops are defined, where the LBM loop is coupled with the FDM loop. The LBM main loop takes care of the momentum transport for the fluid and the particles where two distribution functions are solved for density and temperature [Eqs. (5) and (20)]. In addition, it resolves the motion of the particle through Newton's second law of motion [Eqs. (16) and (17)]. The FDM takes care of the thermal effects of the fluid on the particle and the thermal effects of the particle on the fluid [Eq. (24) or (26)]. Such an algorithm iterates until convergence (steady state is achieved) or the simulation reaches the maximum time period. The coupling between the two methods is implemented based on the response time of the particle. The response time of the particle, also referred to as the relaxation time of the particle, is defined as the ability of the particle to transition between the particle motion state to a different state [47]. However, it is essential to acknowledge that particle dynamics are also influenced by the surrounding fluid flow. To account for these influences, the Stokes number St is utilized as the ratio of the particle relaxation time to the characteristic time scale of the flow. This dimensionless number, as shown in Eq. (34), offers insight into the extent of particle motion relative to the fluid [48]:

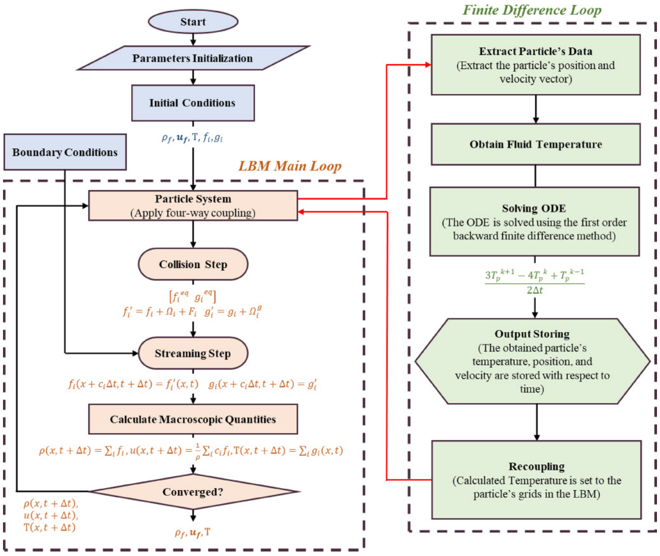

FIG. 2. The algorithmic framework of the current numerical model.

$$\text{St}_p = \frac{\varpi_p}{\varpi_f}. \tag{34}$$

Here, ϖ_f is the characteristic time scale of the flow, and ϖ_p is the particle relaxation time obtained from [47]

$$\varpi_p = \frac{\rho_p {D_p}^2}{18\mu_f}. \tag{35}$$

The value of the Stokes number is divided into two ranges. If $\text{St}_p \ll 1$, then the relaxation time of the particle is minimal in comparison with the scale of the fluid. On the other hand, if $\text{St}_p > 1$, then the particle migrates independently. For this paper, water is utilized as the fluid in the simulation, with the temporal scale of 6 μs, the Stoke's number = 0.002. The value indicates that the particle changes in motion each 500 time steps of the fluid. Based on this, the fluid flowing over the particle will absorb or release the heat dissipated by or to the MPCM particle, and the grids overlapping the particles attain the instantaneous particle temperature.

E. Complete four-way coupling

The physics behind the interaction of the particle with its surroundings is substantial and complex. Mimicking the exact behavior of the particle interaction with the surrounding medium is important for an accurate simulation. Hence, achieving this aim is addressed by introducing the concept of four-way coupling [48,49]. As mentioned earlier, the four-coupling approach considers the MPCM particle collision with the surface of the channel. The particle-wall collision requires a separate treatment to approximate the elastic or inelastic collision of the particle with the solid wall. Several collision models were investigated [50–53] to completely capture the collision dynamics of the MPCM particle and resolve it accurately. Due to its simplicity, the method of Crowe *et al.* [52] has gained attention in the literature [54,55] for predicting the behavior of the particle after the impact. The hard sphere model describes the particle rebound velocity and the before-impact velocity as a ratio called the coefficient of restitution e shown as

$$e = \frac{\mathbf{V}_{\mathbf{y}}^{(2)}}{\mathbf{V}_{\mathbf{y}}^{(0)}}. \tag{36}$$

Superscripts 2 and 0 indicate the conditions after and before the impact of the particle with the wall surface. The model is designed to address postcollision translation and angular velocities in rigid spherical particles. Such physical variables are solved using the impulse equations. Additional information on this subject can be found in Ref. [52]. The essential parameter of the model is the coefficient of restitution e, governing postcollision particle behavior. However, it has limitations in addressing the effect of viscous dissipation upon the impact of the particle with the wall in viscous fluids. In addition, a refined time step is necessary to accurately capture the collision dynamics. Hence, we investigated a second model, namely, the one revealed by Nassauer and Kuna [53]. The model focuses on predicting the behavior of the solid particle collision by obtaining the contact forces from the general contact law that mainly depends on the overlapping volume V_{ol} and indentation depth d_{ind}. This model not only models the interaction of particles with wall surfaces but also the interaction of interparticle collisions. The particle is virtually enlarged and thus defines the overlapping volume as the overlapping section between the virtually enlarged particle and the wall. Following this model, the contact force of the particle-wall collision is obtained from

$$\mathbf{F_c} = \frac{4E^*\sqrt{d_{\mathrm{ind}}V_{\mathrm{ol}}}}{3\sqrt{\pi}}(1 + c\dot{\boldsymbol{d}}), \tag{37}$$

in which c is the damping constant, and $\dot{\boldsymbol{d}}$ is the relative velocity between the particle and wall in contact. The effective modulus of elasticity E^* is described as

$$E^* = \left[\left(\frac{1-\upsilon_A{}^2}{E_A}\right) + \left(\frac{1-\upsilon_B{}^2}{E_B}\right)\right]^{-1}, \tag{38}$$

where E and υ are the modulus of elasticity and Poisson's ratio for the colliding objects A and B, respectively. The other essential exhibited force is the tangential force, also called frictional force, defined as

$$\mathbf{F_t} = \mathbf{F_c}\left[\frac{\mathbf{a}^2(2f_{\mathrm{st}}^* - f_{\mathrm{kin}})}{\mathbf{a}^4 + 1} + f_{\mathrm{kin}} - \frac{f_{\mathrm{kin}}}{\mathbf{a}^2 + 1}\right], \tag{39}$$

with

$$f_{\mathrm{st}}^* = f_{\mathrm{st}}\left[1 - 0.09\left(\frac{f_k}{f_{\mathrm{st}}}\right)^4\right], \tag{40}$$

where f_{st} is the static friction coefficient, and f_{kin} is the kinetic friction coefficient. Also, $\mathbf{a}$ is the ratio between normalized tangential velocity and the transition velocity from static to kinetic friction. In this paper, we emphasize these models to highlight the key parameters that are essential in revealing the dynamics of particle collisions. We precisely analyzed the impact of these key parameters on particle-wall collision physics, finetuning them to accurately simulate the collision dynamics.

TABLE I. The fluid properties of each case in the ten Cate *et al.* [56] experiment.

Case No.	Fluid's density, ρ_f (kg/m^3)	Fluid's dynamic viscosity, μ_f (Pa s)
1	970	0.373
2	965	0.212
3	962	0.113
4	960	0.058

In this paper, the examination of the models of both Crowe *et al.* [52] and Nassauer and Kuna [53] is undertaken. Based on this comparison and considering the limitations associated with the restitution coefficient, we have decided to proceed with the Nassauer and Kuna [53] model. Further details regarding the model comparison can be found in Sec. III D.

III. VALIDATION OF NUMERICAL SCHEME

In this section, we present the validation of this paper for the complete four-way coupling using the single-particle sedimentation, classic DKT investigation, and particle-wall interaction experiment tested by the models of Crowe *et al.* [52] and Nassauer and Kuna [53]. Additionally, the transient thermal behavior of the particle is verified. Lastly, the velocity and thermal profiles of the channel are validated.

A. Sedimentation of a single spherical particle in an enclosure

The first validation case in this paper is a comparison between the current model and the experimental work of ten Cate *et al.* [56] for the sedimentation of a single solid particle in a static incompressible Newtonian fluid. For validation purposes in two-dimensional nonspherical particles or irregular-shaped single-particle sedimentation test cases, it is recommended to refer to the study conducted by Chen *et al.* [57]. The experiment of ten Cate *et al.* [56] encompasses four distinct cases, each involving fluids with varying densities and viscosities. Table I summarizes the details of each case.

The isothermal incompressible fluid is entrapped by a domain sized 0.16 m high and 0.1 m by 0.1 m in width and depth, like that of the experimental setup. Bounce-back (no slip) boundary conditions are applied to the walls of the domain. The density of the particle is selected as 1120 kg/m^3 with a diameter of 15 mm positioned at the center of the rectangular domain at the height of 0.12. The schematic of the problem is illustrated in Fig. 3.

In the LBM model, the domain is divided into 200, 200, and 320 voxels in the x, y, and z axes, respectively. Therefore, the spacing of each grid is set to 0.5 mm. In this validation, the diameter of the particle fits 30 grid cells. The two parameters targeted in this validation are the settling velocity and the vertical location of the particle. Figure 4 plots the accelerated velocity in the direction of gravity against time for all four cases, and Fig. 5 demonstrates the normalized location of

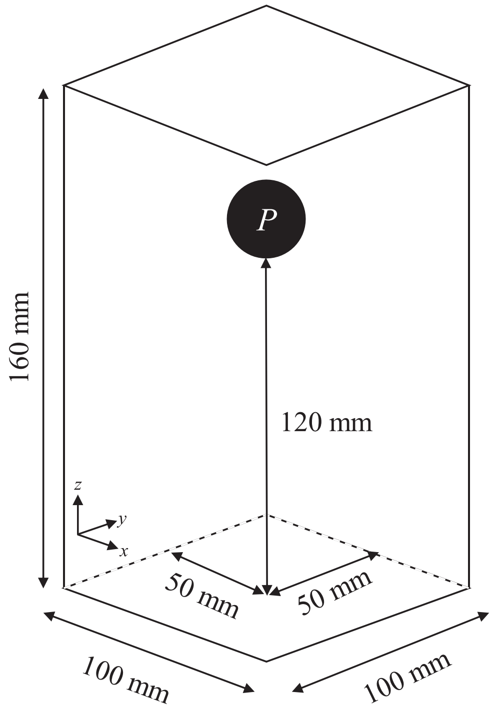

FIG. 3. Schematic for the single-particle sedimentation problem.

the particle in the z direction against time for all four cases. Figures 4 and 5 show good agreement with the experimental findings.

B. Sedimentation of an elliptical particle in a viscous fluid

In this phase of this paper, the behavior of a settling elliptical particle in an infinite channel with width ($8a$) filled with a fluid is represented. Initially, the elliptical particle at rest is located at the centerline of the channel at the angle of $\theta_0 = \pi/2$. The elliptical particle with a density of $1100\,\mathrm{kg/m^3}$ has a major axis (a) length of 0.05 cm and a minor axis (b) length of 0.025 cm. The density and dynamic viscosity of the fluid are $\rho_f = 1000\,\mathrm{kg/m^3}$ and $\nu_f = 10^{-6}\,\mathrm{m^2/s}$, respectively. The gravitational acceleration $\mathbf{g}$ is equal to $9.81\,\mathrm{m/s^2}$, and no-slip boundary conditions are applied on the walls of the channel, as depicted in Fig. 6. The particle is discretized by 9 lattices across the minor axis length and 18 lattices across the major axis length. Furthermore, the time step selected corresponds to $\tau_f = 0.515$. The elliptical particle initiates sedimentation and rotational movement through the channel, eventually stabilizing at a terminal Reynolds number of 6.6. The findings are compared with data obtained from Xia *et al.* [58] and Chen *et al.* [57].

The findings are demonstrated in Fig. 7. Figure 7(a) tracks the lateral migration of the particle with respect to the settling position, and Fig. 7(b) tracks the change in orientation of the

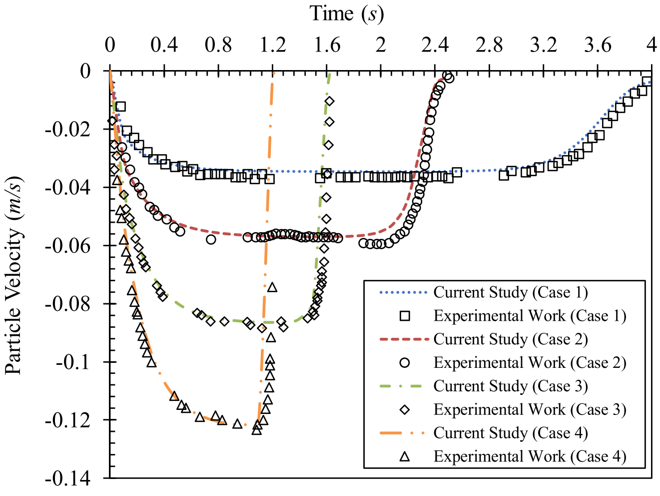

FIG. 4. Streamwise particle velocity vs time in the current model compared with the experimental setup of ten Cate *et al.* [56] for four cases.

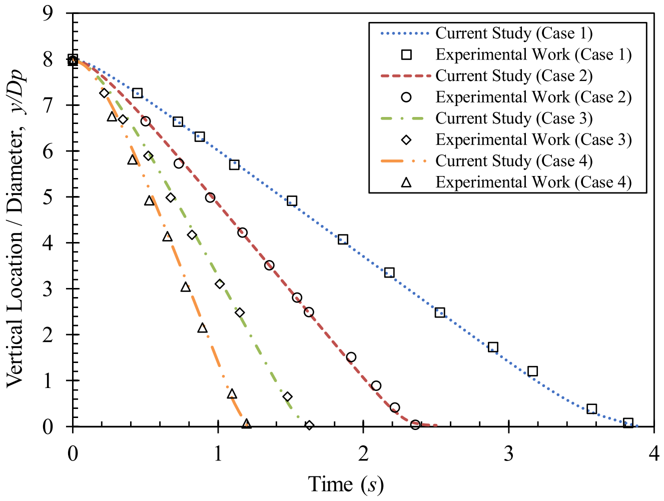

FIG. 5. Normalized vertical particle position plotted against time for the current model along with the findings of the experimental setup by ten Cate *et al.* [56] for four cases.

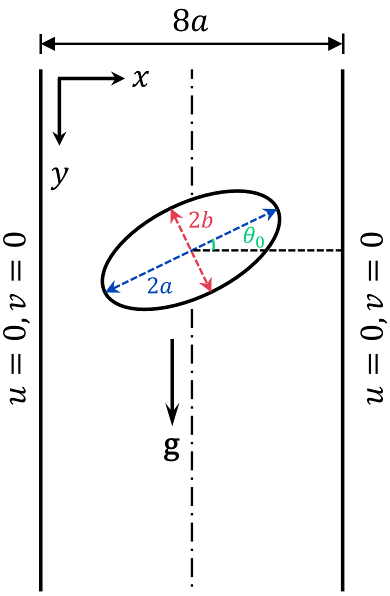

FIG. 6. Schematic for the elliptical particle sedimentation.

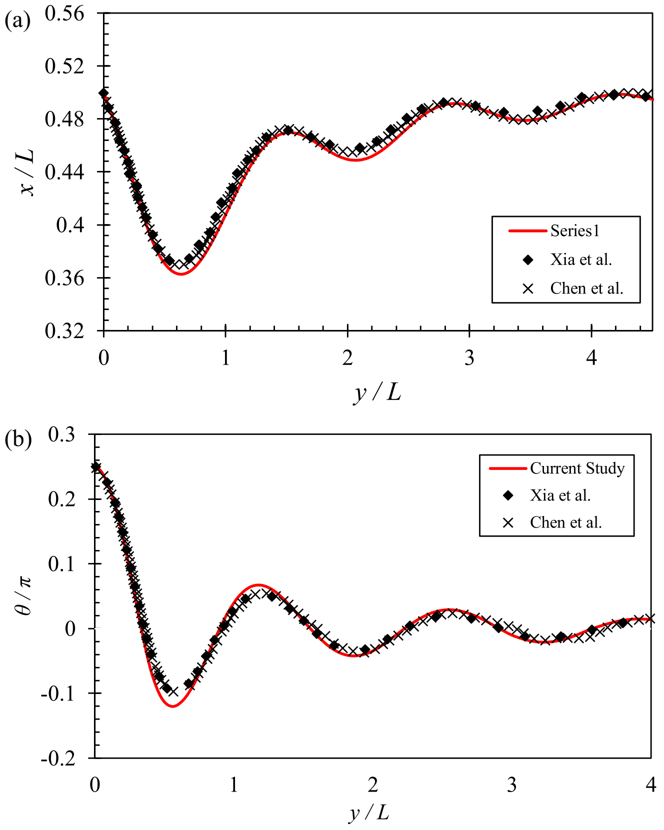

FIG. 7. (a) Particle lateral position and (b) particle orientation plotted against the normalized settling position for the current model along with the findings of Xia *et al.* [58] and Chen *et al.* [57].

particle with respect to the settling position. It is evident that the present results agree well with Xia *et al.* [58] and Chen *et al.* [57] results, and the reported behavior is reproduced.

C. Interaction of two-particle sedimentation in a cavity

The DKT analysis is a benchmark problem where two particles settle in an enclosure filled with a viscous fluid and interact with each other accordingly. Such behavior is recreated to assess the fidelity of the model by comparing this paper against the numerical works of Wang *et al.* [59], Nie *et al.* [60], Krause *et al.* [26], and Feng and Michaelides [61]. The setup involves water ($\rho_f = 1000\,\mathrm{kg/m^3}$ and $\nu_f = 10^{-6}\,\mathrm{m^2/s}$) as the fluid medium. The two particles with identical radii of 1 mm and a density of $1010\,\mathrm{kg/m^3}$ are placed in a $2 \times 8-$cm $-$ high two-dimensional domain (Fig. 8). The upper particle is positioned at $\{0.999, 7.2\}$ cm, and beneath it is the leading particle with a position of $\{1,\ 6.8\}$ cm. The fluid is stagnant and isothermal, and no-slip boundary conditions are applied to the walls of the domain.

The domain of the model is discretized into 1600 grids on the x axis and 6400 grids on the y axis. Hence, the lattice spacing is 12.5 μm. The particle-particle collision parameters are obtained from the study of Zhang *et al.* [62] due to the absence of experimental data for these specific parameters. The critical finding targeted in this validation is the lateral motion of the particles rather than the vertical motion, as this was validated in the previous section. Initially, the two particles start to sediment across the fluid (drafting). Afterwards, the particle collides (kisses) at $t = 1.5$ s, where the trailing particle pushes the leading particle to the side and then initiates the tumbling part at 2.5 s.

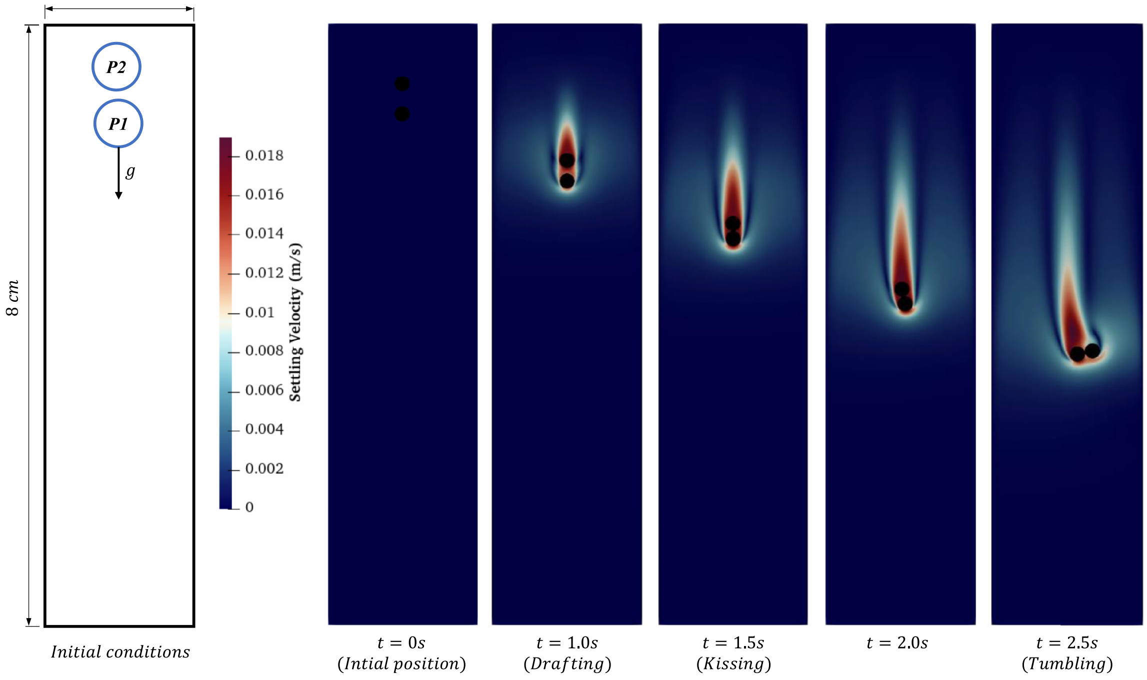

FIG. 8. The schematic on the left-hand side represents the two-particle interaction problem. P1 and P2 denote the leading and trailing particles, respectively. Contours on the right-hand side of the figure show the drafting-kissing-tumbling timeframes.

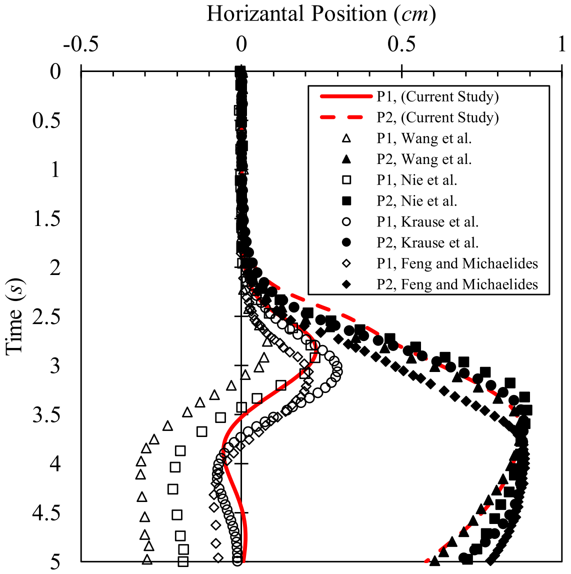

FIG. 9. Particle lateral position over time: a comparative analysis with literature (Wang *et al.* [59], Nie *et al.* [60], Krause *et al.* [26], and Feng and Michaelides [61]). Filled symbols denote the leading particle, and unfilled symbols represent the trailing particle.

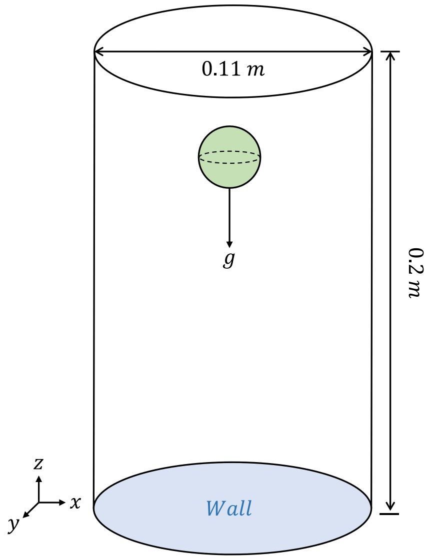

FIG. 10. Validation setup for particle-wall contact model.

The comparison between the findings of this paper and several published works in the literature is demonstrated in Fig. 9. The graph presents the behavior of both particles in the lateral direction for the range of 5 s. The investigation into the DKT dynamics of two particles presents a complex challenge, as highlighted by the inconsistencies in existing research, notably in Fig. 9. This complexity arises from the variability in both particle-particle and particle-wall interaction parameters. A critical aspect of accurately representing the physics of DKT phenomena involves the precise adjustment of these parameters. The studies compared in Fig. 9 did not provide detailed values for these parameters, and each referenced study utilized distinct models with varying parameters. This discrepancy in parameters contributes to the observed differences in the results reported by various researchers, particularly noticeable in the tumbling phase of particle transport. It is important to note that the availability of experimental data for the two-dimensional DKT model would enable finer calibration of the parameters of these studies to align with empirical findings. However, such data are currently not available.

D. Rebound motion of a particle near the bottom surface

This subsection involves the validation of the particle-wall interaction by two models, namely, the particle-wall interaction method of Crowe *et al.* [52] and the discrete contact model [53], using the experimentation of Hagemeier *et al.* [63]. The experiment involves a Teflon particle with a diameter of 20 mm suspended in a cylindrical tank with a radius of 55 mm filled with a water-glycerin mixture ($\rho_f = 1141\,\mathrm{kg/m^3}$ and $\mu_f = 0.008\,\mathrm{kg\,m^{-1}\,s^{-1}}$) shown in Fig. 10. According to the studies [64,65], polytetrafluoroethylene (PTFE) spheres have a density of $2170\,\mathrm{kg/m^3}$, a modulus of elasticity of 0.670 GPa, and Poisson's ratio of 0.46. The static and kinetic friction factors are obtained from the same studies and are reported as 0.05 and 0.02, respectively. The domain is discretized by 100 grids in the x axis for adequate results. For the model of Crowe *et al.* [52], the restitution coefficient is selected with a value of 0.72 according to Hagemeier *et al.* [63]. In addition, the time step size for the same model is selected as 10^{-4} s. On the other hand, the discrete contact model is employed with a damping constant of 0.05. The parameters of the discrete contact model are selected according to the recommendation of Marquardt *et al.* [66].

Having the numerical setup, the spacing between the bottom surface of the particle and the wall is plotted in Fig. 11. As shown in Fig. 11, a discrepancy is observed during the initial sedimentation stage before the particle-wall collision. This early stage, where particle-wall interaction is yet to occur, suggests that the deviation might be related to issues in the free sedimentation of the particle. The aspect of free sedimentation was previously tested and validated, as evidenced

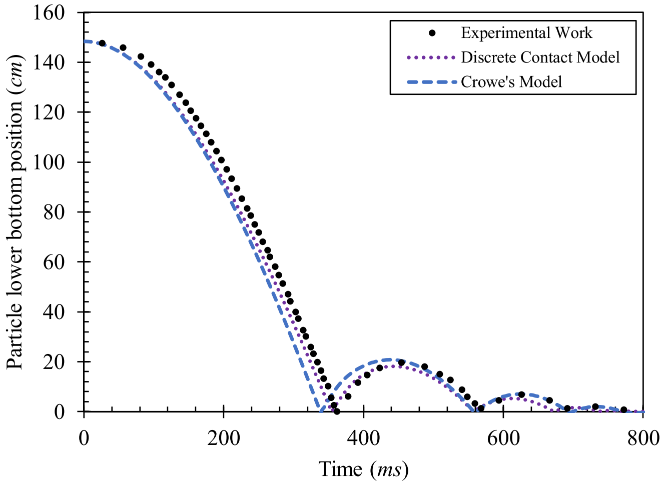

FIG. 11. Validation of particle rebound height for discrete contact model [53] and the model of Crowe *et al.* [52] with experimental work [63].

TABLE II. Thermophysical properties of particles utilized in the validation of a hot particle.

Particle material	Density, ρ_p (kg/m^3)	Specific heat capacity, C_p (kJ K^{-1} kg^{-1})
Aluminum	2702	0.903
Beryllium	1850	1.825

in Figs. 4 and 5. Interestingly, the validation shown in these figures (Figs. 4 and 5) aligns more closely with the experimental data than the comparisons made in Fig. 11. This indicates that uncertainties in the experimental data, particularly those presented in Fig. 11, may contribute to the observed discrepancy. Furthermore, the differences noted before and after the rebound appear to be independent of the accuracy of the discrete contact model [53] or the model of Crowe *et al.* [52]. In the upcoming analysis, the discrete contact model was adopted for this paper, as it captures the rebound physics more appropriately. Additionally, it does not require any treatment for the time step size.

E. Transient thermal response of a hot particle in a cavity

To evaluate the thermal reliability of the proposed hybrid LBM-FDM model, a hot metallic spherical particle with an initial temperature of 350 K is suspended, initially stationary in a rectangular container constructed like the Cate *et al.* [56] experiment, filled with the fluid with properties demonstrated in Case 1 of the Cate *et al.* [56] experiment. Aluminum and beryllium were used as the materials of the spherical particles, each with a diameter of 1 mm. The thermophysical properties are summarized in Table II. Since the maximum Biot number obtained in this analysis is 0.001, the analytical solution shown in Eq. (41) is compared with the current hybrid LBM-FDM model. For the LCM, the nondimensional temperature across the solid spherical particle is estimated using [67]

$$\theta = \frac{T(t) - T_\infty}{T_{p,\mathrm{sf}} - T_\infty} = \exp\left(-\frac{t}{\tau_{\mathrm{LCM}}}\right), \tag{41}$$

where θ indicates the nondimensional temperature. The subscripts w and ∞ represent the surface of the particle and surrounding fluid, and τ_{LCM} is the thermal time constant obtained from

$$\tau_{\mathrm{LCM}} = \frac{U_p A_{\mathrm{sf}}}{\rho_p V C_p}, \tag{42}$$

where A_{sf} and V are the surface area and volume of the sphere. Since the particle suspension is validated in the preceding section, the suspending velocity of the particle is used as an input to Eq. (41). The primary focus of the investigation lies in evaluating the efficacy of the proposed model in accommodating variations in the temperature of the particle. As depicted in Fig. 12, the submerged particle exhibits an exponential energy loss to the encompassing fluid. The associated graph provides insights into the temporal reduction of the temperature of the particle from its initial state to that of the surrounding fluid. Eventually, after a long period, the particle attains thermal equilibrium with the ambient surroundings. The duration of this thermal equilibration is contingent upon the thermophysical properties of the particle. For instance, in the case of the beryllium material, characterized by its high specific heat capacity, the energy dissipation rate of the particle is notably low. This behavior can be attributed to the increased thermal time constant, which indicates a delayed response to changes in its thermal environment. The gradual decay behavior is accurately achieved by the model and does not require any finer time step. Similarly, the model accurately predicts the thermal behavior of aluminum, a material characterized by lower heat capacity yet higher thermal conductivity. Fundamentally, the results of the model align favorably with analytical solutions, demonstrating the effectiveness in simulating particle-fluid thermal interactions.

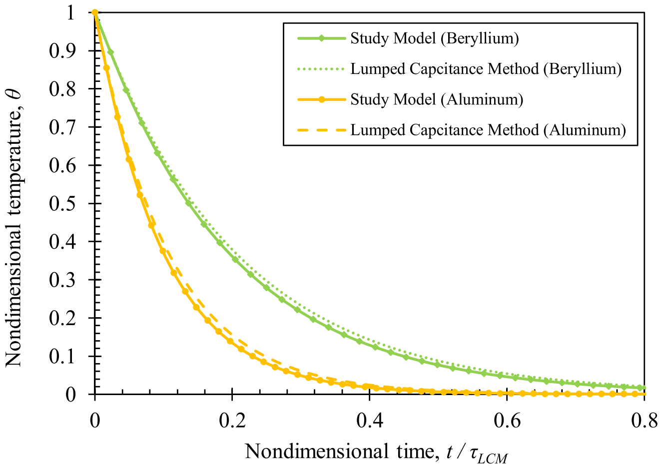

FIG. 12. Comparison between the hybrid numerical method with the closed form solution.

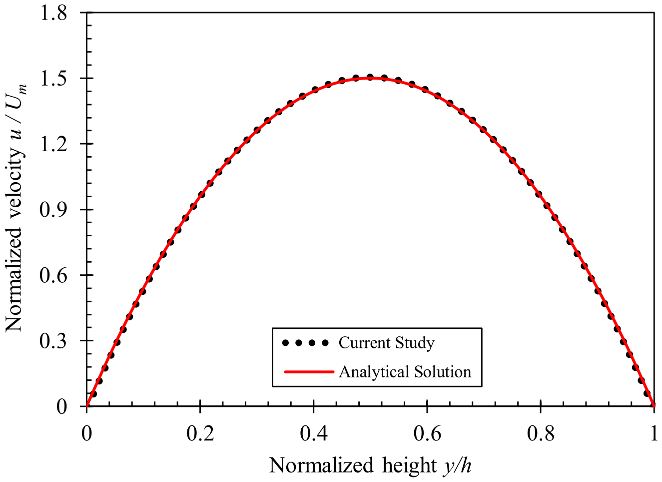

FIG. 13. The fully developed velocity profile across the height of the channel obtained using the analytical solution against the current model.

F. Hydrodynamic and thermal behavior of a minichannel flow

Through the previous sections, the physics governing the kinetics and thermal dynamics of the resolved particle has been thoroughly addressed. Nonetheless, it is also critical to substantiate the flow domain in both the momentum and energy fields. To accomplish that, the analytical solution of a flow between two parallel plates is provided for the velocity as [68]

$$\mathbf{V}(y) = \frac{3}{2}\mathbf{u_m}\left\{1 - \left[\frac{y^2}{(0.5h)^2}\right]\right\}, \tag{43}$$

where $\mathbf{u_m}$ is the channel mean velocity, h or H is the height of the channel, and y is the varying distance from the channel center. The channel Reynolds number is defined based on the hydraulic diameter, $\mathrm{Re}_{D_h} = \frac{D_h\,\mathbf{u_m}}{\nu}$, where D_h is the hydraulic diameter and is equivalent to twice the height of the channel. With a heat flux boundary condition imposed on the two parallel plates, the local Nusselt number of the channel surface (Nu_x) is utilized to indicate the variation of the Nusselt number along the length of the channel. Therefore, the local Nusselt number of the channel surface in the entrance and developed region is represented by [68]

$$\mathrm{Nu}_x = \begin{cases} \frac{1.49}{x_*^{1/3}}, & x_* \leqslant 0.0002, \\ \frac{1.49}{x_*^{1/3}} - 0.4, & 0.0002 < x_* \leqslant 0.001, \\ 8.235 + 8.68e^{-164x_*}(x_* \times 10^3)^{-0.506}, & x_* > 0.001. \end{cases} \tag{44}$$

Here, x_* is the nondimensional entrance length obtained from $x_* = \frac{x/D_h}{\mathrm{Re}_{D_h}\mathrm{Pr}}$, in which Pr is the Prandtl number. For the findings of the numerical model, Nu_x is obtained from

$$\mathrm{Nu}_x = \frac{q''(x)D_h}{k_f[T_{\mathrm{sf}}(x) - T_m(x)]}, \tag{45}$$

where q'' represents the applied heat flux, T_{sf} is the local surface temperature, and T_m is the bulk temperature at a certain local distance obtained using

$$T_m = \frac{1}{H \cdot \mathbf{u_m}} \int \mathbf{u}T\,dy, \tag{46}$$

with

$$\mathbf{u_m} = \frac{1}{H} \int \mathbf{u}\,dy, \tag{47}$$

where H represents the height of the channel. The fluid is water with a Pr of 6.4 flowing with $\mathrm{Re}_{D_h} = 594$. The channel height is 4 mm, and the length is set to achieve a fully developed flow. The two walls of the channel use a bounce-back scheme with constant heat flux applied at each wall. The inlet and outlet of the channels employ the Dirichlet boundary condition to the inlet (constant velocity) and outlet (zero pressure) of the channel. In the setup of the parameter, the mesh size is 0.0202 mm with a time step of 9.16 µs for stability and high accuracy. Accordingly, the velocity profile at the developed local distance is plotted compared with the analytical solution [Eq. (43)] in Fig. 13. Correspondingly, the local Nusselt number obtained by Eq. (44) is plotted against the numerical model, as shown in Fig. 14. The figure demonstrates our ability to model the developing flow (Graetz problem) and the fully developed region for a flow between the parallel plates. The analogy reveals the competency of the model in handling the channel flow of fluid motion accompanied by heat transfer with a minor error percentage.

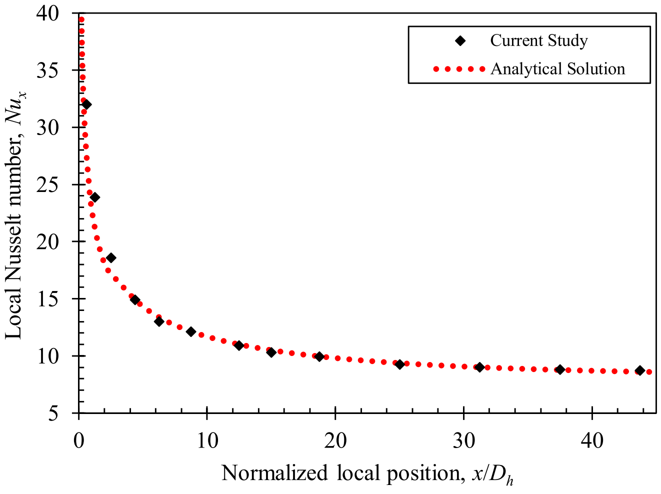

FIG. 14. The distribution of the local Nusselt number across the normalized local length of the channel is obtained using both the analytical solution and the current model.

In summary, the hybrid LBM-FDM model has undergone thorough testing and has been demonstrated to be a reliable model for simulating thermal transport in suspensions under both steady-state and transient conditions.

G. Mesh independence analysis

In computational simulations, it is important to ensure the independence of the findings from the grid size, and such an analysis enables us to achieve adequate accuracy with efficient run time. Typically, LBM simulations employ a

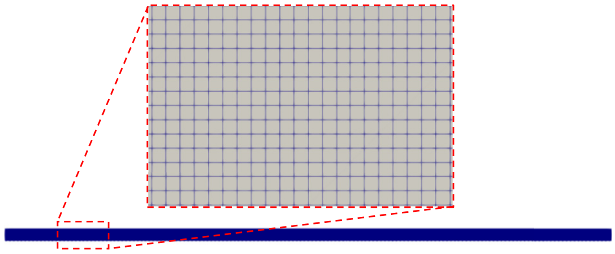

FIG. 15. Visualization of the computational mesh generated for the model.

TABLE III. Mesh sensitivity analysis for various mesh types.

Mesh type	Very coarse	Coarse	Baseline	Fine
Number of grids, $x \times y$	50 × 2475	100 × 4950	200 × 9900	400 × 19800
Grid size (μm)	80.8	40.4	20.2	10.1
Nusselt number at fully developed location, Nu_x	10.302	9.033	8.351	8.235
Relative error (%)	25.1	9.69	1.41	—

square grid mesh that exhibits uniformity across the entire computational domain. This uniformity simplifies the mathematical implementation of the simulation process. Although LBM simulations can accommodate various mesh shapes to address complex geometries, in the context of this paper, where the geometric characteristics of the domain remain relatively simple, the utilization of a uniform square grid suffices, as demonstrated in Fig. 15, and such a uniform mesh geometry was used for all the rigorous validation that we presented in the last section. The mesh sensitivity analysis targeted the nondimensional number Nu_x at the fully developed location as the main parameter for comparison in a convective flow with no MPCM particles. As demonstrated in Table III, four types of meshes—very coarse, coarse, baseline, and fine—are examined to identify the most efficient mesh size. The very coarse and coarse meshes, with typical sizes of 80.8 and 40.4 μm, respectively, were deemed to be insufficient for fully resolving the hydrodynamic and thermal behavior of the findings. The fine mesh, while accurate, proved to be computationally expensive when the microparticles were employed. Therefore, the baseline mesh is employed in this paper (where the deviation between the fine and the baseline is <1.5%, as shown in Table III). Such a selection provides the particle with 8 grid cells in diameter to inhibit during the analysis.

IV. RESULTS AND DISCUSSION

A. Physical model and slurry viscosity estimation

In this paper, the MPCM particles are suspended in a carrier fluid of mainly water to investigate the potential of the suspension in enhancing heat transfer. The presence of microparticles influences the properties of the carrier fluid. Commonly, the viscosity of the slurry is estimated using either the Einstein [69] or the Brinkmann [70] model. However, such correlations presume homogenous dispersion of the microparticles, which is not completely true when dealing with random microparticle dispersions. Therefore, to estimate the viscosity of the slurry, a detailed analysis is conducted. A large foreign sphere is dropped in an enclosed rectangular container filled with a slurry of various volume fractions. Figure 16 is a representation of this analysis setup. The properties, the size of the large sphere, and the dimension of the numerical domain are like Case 1 of the Cate *et al.* [56] experiment. The foreign particle is initially at rest and initiates its descent at $t > 0$. As it descends, the foreign particle eventually reaches its terminal velocity and ceases to accelerate, a condition attained through the balance of the net forces acting upon it. At this period, the terminal velocity is determined by the equilibrium between the gravitational force (weight), buoyant force, and drag force, giving rise to the following equation:

$$\mathbf{V_t} = \sqrt{\frac{4gD_{fp}}{3C_{\mathrm{dr}}}\left(\frac{\rho_{fp}-\rho_f}{\rho_f}\right)}, \tag{48}$$

where the subscript fp designates the specific parameters that pertain to the foreign particle. Here, C_{dr} is the drag coefficient obtained by the Abraham [71] correlation as

$$C_{\mathrm{dr}} = \left(0.5407 + \sqrt{\frac{24}{\mathrm{Re}_{fp}}}\right)^2, \quad 0 < \mathrm{Re}_{fp} < 5000, \tag{49}$$

with

$$\mathrm{Re}_{fp} = \frac{\rho_f\,\mathbf{V_t}\,D_{fp}}{\mu_f}, \tag{50}$$

where Re_{fp} corresponds to the Reynolds number of the foreign particle. Solving Eqs. (48)–(50) at the terminal condition with the terminal velocity value obtained from the model simulation provides the dynamic viscosity of the slurry. This process results in the generation of Fig. 17, depicting variations for volume fractions of 0.1, 0.2, 0.4, and 0.8%, respectively. The obtained results are presented as a ratio between the viscosity of the slurry and the viscosity of the base fluid.

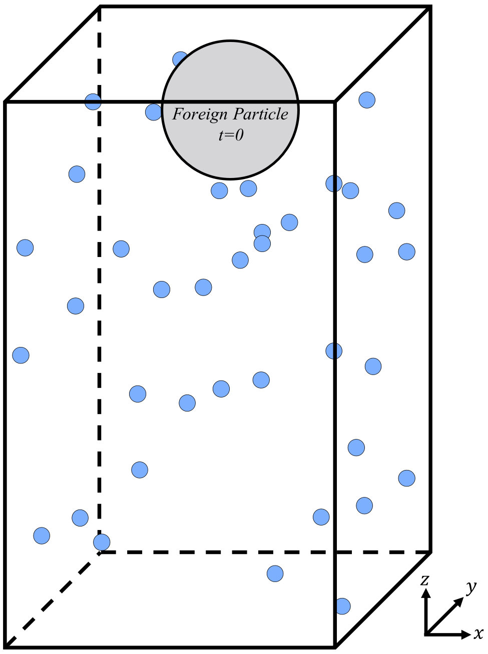

FIG. 16. A depiction of the setup for obtaining the viscosity of the slurry.

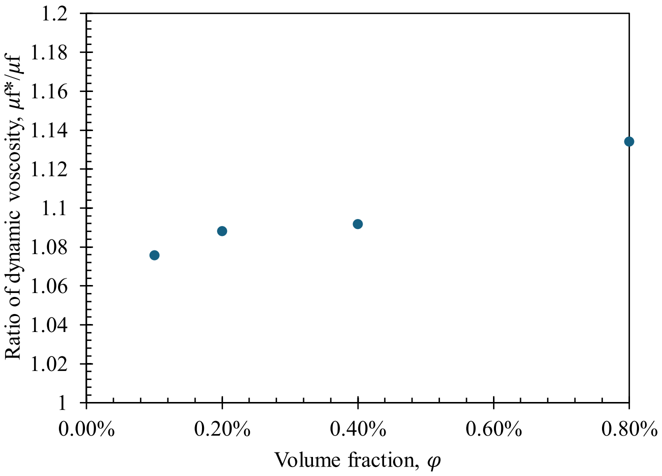

FIG. 17. Ratio of dynamic viscosity to that of the base fluid for varying volume fractions.

Through Fig. 17, the model demonstrates its efficacy in capturing the influence of MPCM particles on fluid viscosity. While the viscosity test employed a dispersed particle configuration throughout the enclosure, the current model exhibits versatility in handling regions where the volume fractions significantly vary. As a result, in this paper, we provide a valuable tool for investigating particle distribution in different regions within the channel, such as the top wall, bottom wall, or centerline.

Consequently, the results of this paper are divided into two primary segments. The first part examines three distinct cases of MPCM particles at $\mathrm{Re}_{Dh} = 200$, which are categorized as follows: light MPCM particles [11] ($\rho_p < \rho_f$), heavy MPCM particles [72] ($\rho_p > \rho_f$), and neutrally buoyant MCPM particles [73] ($\rho_p \approx \rho_f$). The second segment investigates the influence of various parameters for a single case of MPCM particles. The MPCM particles for this whole paper are spherical and rigid with constant impact parameters (E^*, f_{st}, f_{kin}, and υ; Sec. II E). Moreover, the particles possess an 80 μm radius and are positioned within an incompressible, two-dimensional laminar flow regime. Figure 18 provides a comprehensive description of the current analysis setup with the necessary boundary and initial conditions. A time step of 1 μs was determined to yield results independent of the time step across the entire range of volume fractions. Therefore, it is utilized in this paper. The particle-wall impact parameters are selected based on the recommendation of Marquardt *et al.* [66]. The simulations are conducted on a high-performance computing cluster at Khalifa University, utilizing Intel Xeon Gold 6230R processors. Each simulation is conducted utilizing 50 processing cores, with each case requiring approximately one week for completion.

B. Impact of MPCM particle distribution

The steady-state distribution of the MPCM particles in a confined minichannel is contingent upon their density, resulting in either sedimentation at the lower or upper regions, or potentially in between, of the surface of the channel. The distinctive sedimentation patterns exhibited by different MPCM variants are depicted in Fig. 19. A showcase for the comparison between the three cases of MPCM particles is conducted at $\mathrm{Re}_{Dh} = 200$. Typically, for the case of clear fluid with no suspension, the local mean temperature and surface temperature increase along the channel length. Nonetheless, with the presence of the sedimented MPCM particles on the surface of the channel, a major change in the behavior occurs. To give more insight into such variation, the temperature difference between the inlet temperature T_i and the wall temperature T_{sf} is plotted in Fig. 20. Figure 20 demonstrates the growth in the difference in temperature ($T_{\mathrm{sf}} - T_i$) across the streamwise direction of the channel for the three different cases of MPCMs. The neutrally buoyant MPCM particles had the least effect on the surface temperature for all volume fractions. Such behavior is expected since these particles rarely engage with regions of elevated temperatures near the surface of the heating walls [Figs. 21(a) and 21(b)]. Figure 21 demonstrates the nondimensional temperature contours obtained by subtracting the inlet temperature and dividing by the difference between the maximum surface temperature and the inlet temperature $(T - T_{\mathrm{in}})/(T_{\mathrm{sf,max}} - T_{\mathrm{in}})$. This is interpreted in Fig. 20, where the difference between the bottom and top

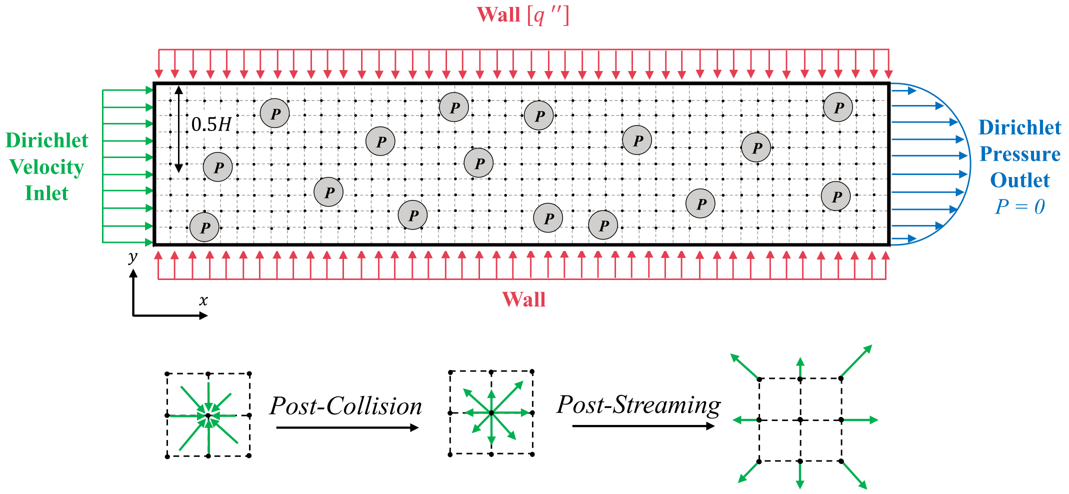

FIG. 18. An illustration of the current model setup with the applied boundary conditions. Note: The particles are not drawn to scale.

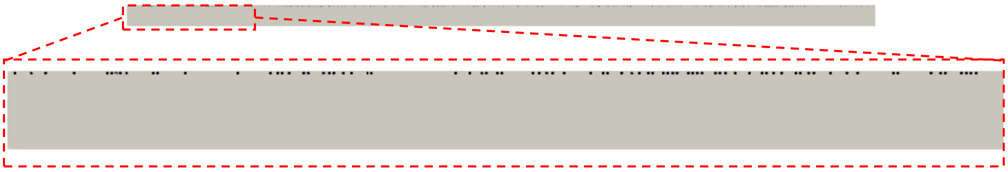

Light MPCM particles ($\rho_p < \rho_f$)

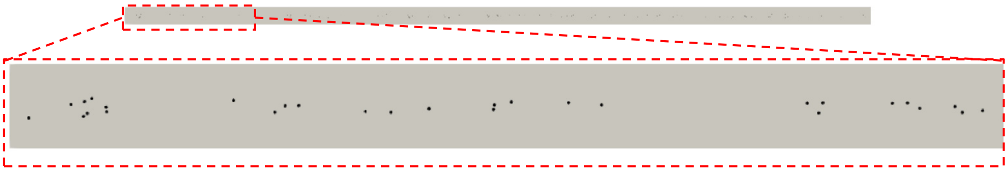

Neutrally buoyant MCPM particles ($\rho_p \approx \rho_f$)

Heavy MPCM particles ($\rho_p > \rho_f$)

FIG. 19. Distinctive sedimentation patterns exhibited by relatively light, neutrally buoyant, and heavy micro-phase-change-material (MPCM) particles.

surface temperatures is zero (as indicated by the black solid and dashed lines). A noteworthy observation regarding the neutrally buoyant MPCM particles pertains to their effect on the thermal behavior of the channel in response to changes in volume fraction. When the volume fraction increased from 0.1 to 0.2%, there was no visible impact on the surface temperature. However, as the volume fraction further increased to 0.4% and subsequently to 0.8%, a notable reduction of 0.5 and 1.1 K, respectively, in surface temperature was observed when compared with the 0.1% volume fraction. The inclusion of more particles led to a more crowded concentration of MPCM particles in the central region, increasing interparticles collisions. Accordingly, these collisions enable the particles to migrate near the regions closer to the walls of the channel and thus decrease the surface temperature [Fig. 21(c)].

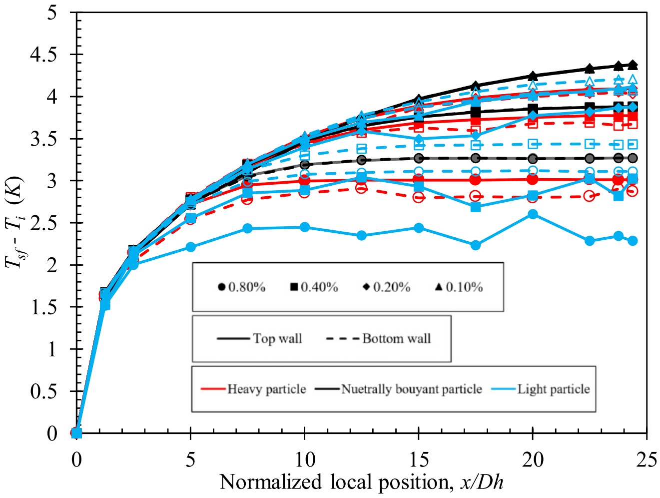

FIG. 20. A diagram illustrating the different behaviors of heavy [red (dark gray)], neutrally buoyant [black], and light [blue (light gray)] micro-phase-change-material (MPCM) particles for different volume fractions at various points of the normalized local position.

In comparison with the neutrally buoyant particles, the heavy MPCM particles had a significant influence on the surface temperature of the bottom walls but a slight impact on the surface temperature of the upper wall. This is attributed to the increased particle concentration within the lower region as opposed to the upper region of the channel surface [Figs. 22(a) and 22(b)]. The MPCM particles in contact with the bottom heating wall absorb the generated heat in the form of latent and sensible energy, and thus, an effective approach in dissipating the heat is provided. Furthermore, due to the increased surface area of the particle, the heat transfer mechanism is further enhanced, resulting in the reduction of the surface temperature. As demonstrated in Fig. 20, such surface temperature reduction is increased by the addition of more MPCM particles in the form of volume fraction. It is important to note that this assertion is specifically applicable to volume fractions exceeding 0.4%, as very minimal influence is visible below this threshold. The surface temperature of the upper walls is also influenced by the presence of the MPCM particles. A similar increase in volume fraction led to the reduction of the upper wall surface temperature by an average of 0.15 and 0.59 K and a maximum of 0.32 and 1.1 K, respectively, when compared with the top surface temperature of 0.1%. The widening gap demonstrated in Fig. 20 between the surface temperatures of the bottom and top walls is directly associated with the increasing number of particles. This behavior occurs

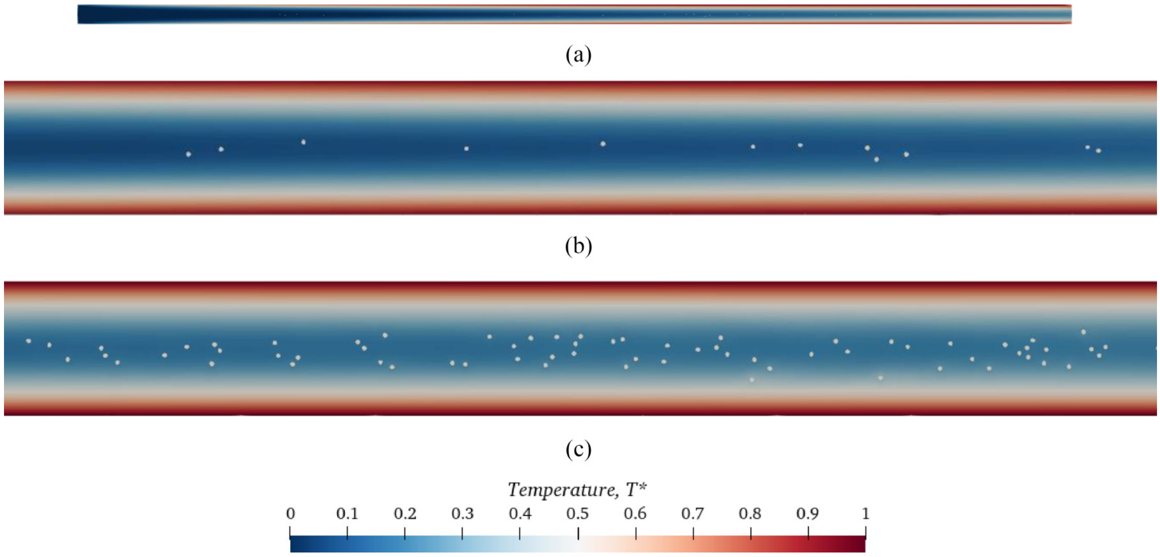

FIG. 21. Normalized temperature contour for the neutrally buoyant micro-phase-change-material (MPCM) particles. (a) Normalized temperature for the full channel at $\mathrm{Re}_{Dh} = 200$. (b) A segment of the channel for the volume fraction of 0.1%. (c) A segment of the channel for the volume fraction of 0.8%.

due to the introduction of a greater quantity of MPCM heavy particles, which in turn intensifies the cooling effect on the surface temperature of the bottom wall. Consequently, this increased cooling effect leads to a more pronounced difference between the temperature values of the two walls.

The last MPCM examined in this analysis is the light MPCM particles. Since these particles exhibit a lower density than the other MPCM cases, the particle distribution is focused on the upper region of the channel. Thus, the surface temperature of the top wall is less than the bottom, as illustrated in Fig. 21. The behavior of the light MPCM particles closely mirrors that of dense MPCM particles in terms of their effect on reducing the surface temperature with increasing particle concentration. However, this effect is negligible at lower volume fractions, specifically at 0.1%. A notable shift in the reduction of the upper wall temperature is observed, with average values of 0.15, 0.67, and 1.07 K for volume fractions of 0.2, 0.4, and 0.8%, respectively, in comparison with the 0.1% volume fraction. The maximum reduction in upper wall temperature for each of these volume fractions across the entire length of the channel is quantified at 0.4, 1.28, and 1.83 K, respectively, when compared with the 0.1% volume fraction. Unexpectedly, the fluctuations of the surface temperature for the volume fraction of 0.8 and 0.4% are more

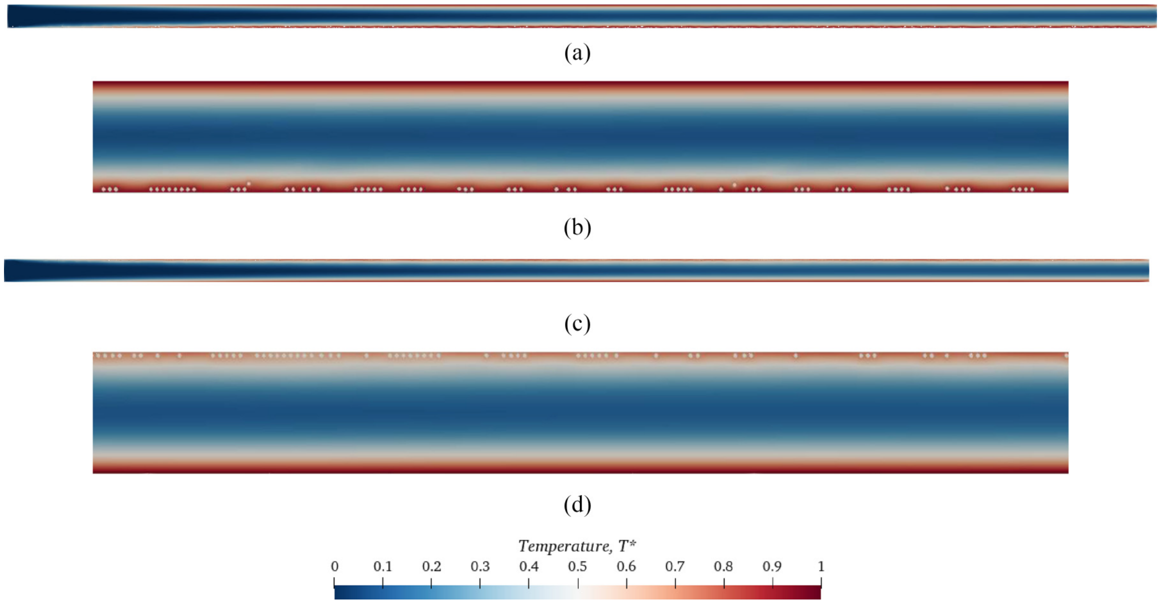

FIG. 22. Normalized temperature contours for various conditions: (a) Heavy micro-phase-change-material (MPCM) particles in the full channel at $\mathrm{Re}_{Dh} = 200$. (b) A 0.1% volume fraction of heavy MPCM particles in a channel segment. (c) Light MPCM particles in the full channel at $\mathrm{Re}_{Dh} = 200$. (d) A 0.8% volume fraction of light MPCM particles in a channel segment.

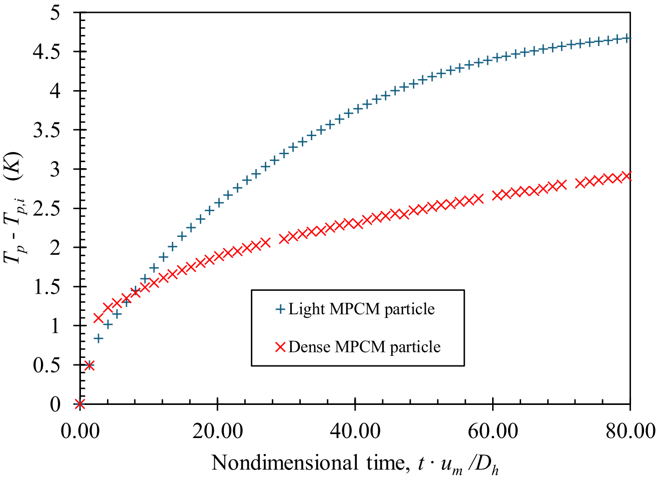

FIG. 23. Comparative analysis of temperature rate change in light and dense micro-phase-change-material (MPCM) particles.

visible compared with the denser MPCM particles at the same volume fractions. The primary reason for this observed behavior is attributed to the difference in densities between the MPCM particles and the surrounding fluid. In the case of light MPCM particles, their faster arrival at the channel surface, when compared with the denser particles, is a consequence of the difference in density between the fluid and the light particles ($\rho_{p,\mathrm{light}} - \rho_f > \rho_{p,\mathrm{heavy}} - \rho_f$). This huge difference, in turn, hinders the uniform dispersion of microparticles along the upper wall of the channel. Therefore, regions without any MPCM particles exist [Fig. 22(d)], leading to no reduction in surface temperature, as outlined by the dashed lines in Fig. 22(d). To understand more why the surface temperature reduction is different for the light and heavy MPCM particles, Fig. 23 is plotted.

Figure 23 demonstrates the particle temperature rate of change for the two cases. The curve represents a random light and dense MPCM particle behavior from its initial state until a certain period. In both scenarios, the MPCM particles absorb heat, resulting in a consequent temperature rise. Because our PCM model accounts for the temperature change during the melting period, the temperature of the particle continues to escalate until it exits the channel. As mentioned before, the lighter MPCM particles approach the heating wall earlier than the dense particles, and thus, the light particles interact with elevated temperature regions more frequently than the dense particles. Moreover, it is noteworthy that the thermophysical characteristics of the light MPCM present distinct advantages when set against the dense MPCM. These reasons enabled the best reduction in surface temperature for light MPCM particles.

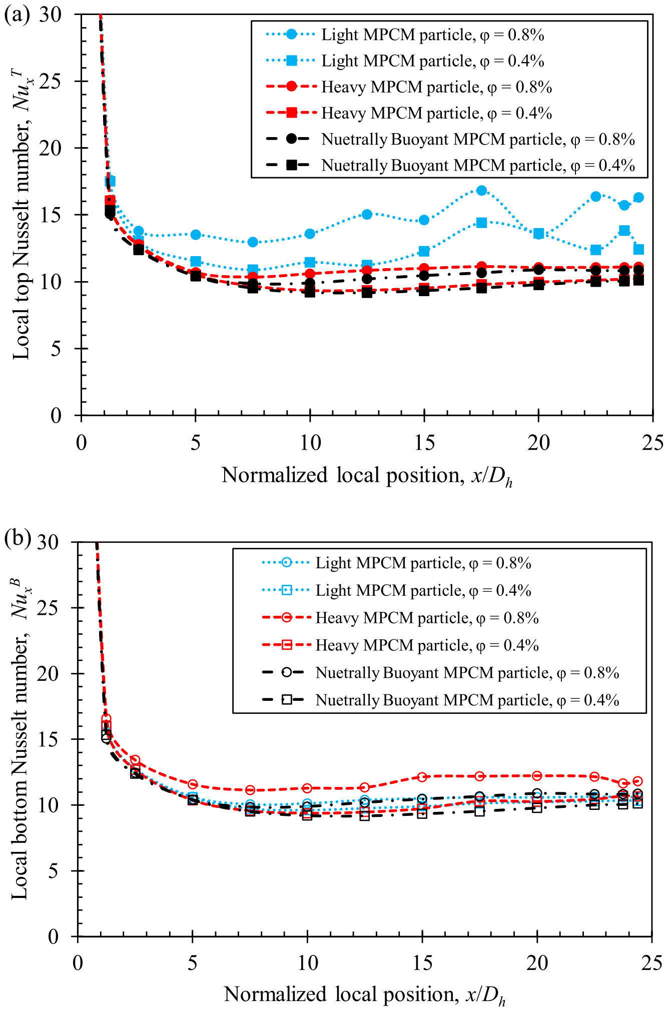

FIG. 24. The distribution of local Nusselt numbers for (a) upper local Nusselt number $\mathrm{Nu}_x^{\mathrm{T}}$ and (b) bottom local Nusselt number $\mathrm{Nu}_x^{\mathrm{B}}$.

C. Effect of particle distribution on heat transfer coefficient

In the channel validation case (Sec. III F), Nu_x is equal for both the top and bottom walls of the channel. Nonetheless, in this section, the presence of particles disrupts this uniformity. Therefore, we introduce a complementary definition of the local Nusselt number, denoted as $\mathrm{Nu}_x^{\mathrm{T}}$ for the top surface and $\mathrm{Nu}_x^{\mathrm{B}}$ for the bottom surface of the channel. These values are determined using the following equations:

$$\mathrm{Nu}_x^{\mathrm{T}} = \frac{-D_h}{T_{\mathrm{sf}}(x) - T_m(x)} \left(\frac{\partial T}{\partial y} \right)_{y=H}, \tag{51}$$

$$\mathrm{Nu}_x^{\mathrm{B}} = \frac{-D_h}{T_{\mathrm{sf}}(x) - T_m(x)} \left(\frac{\partial T}{\partial y} \right)_{y=0}. \tag{52}$$

Using these two equations, the local Nusselt number at the top $\mathrm{Nu}_x^{\mathrm{T}}$ and bottom $\mathrm{Nu}_x^{\mathrm{B}}$ surfaces of the channel are evaluated, as shown in Fig. 24. Based on the prior findings, we anticipated the specific trends in the Nusselt numbers for the bottom and upper channel walls concerning light, neutrally buoyant, and heavy MPCM particles. These trends are dependent upon the local surface temperature. However, it is essential to acknowledge that the Nusselt number is additionally influenced by both the average local temperature and the temperature gradient along the height of the channel. In light of this, the local heat transfer coefficient for the neutrally buoyant MPCM particles increased, and that is attributed to the influence on the bulk fluid temperature and not the surface temperature. As demonstrated in Fig. 22(d), the effect of the light MPCM particle is more influential than the other two types. That is

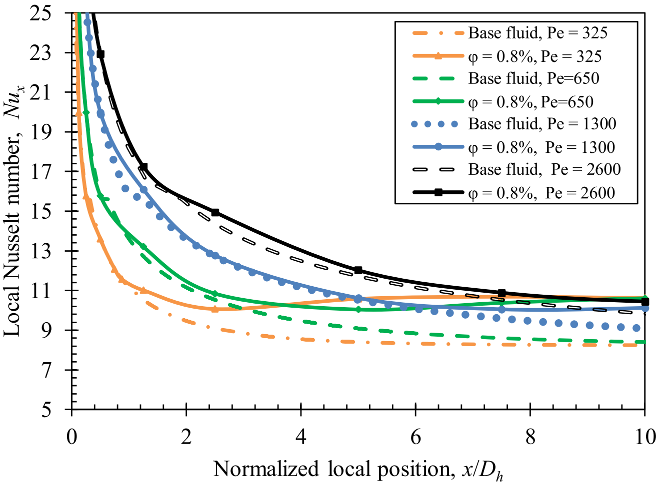

FIG. 25. A compilation of local Nusselt number trends is presented at the entrance region, portraying the relationship with nondimensional local position and volume fraction, characterized by Peclet number.

the reason why the local Nusselt number for the upper heating surface is significant. Naturally, this observed behavior becomes more pronounced with the increased incorporation of additional MPCM particles for the three MPCM cases, as depicted in Fig. 24. Furthermore, the fluctuations in $\mathrm{Nu}_x^{\mathrm{T}}$ for the light MCPCM particles are ascribed to the fluctuation in surface temperature.

D. Influence of volume fraction on heat transfer enhancement

Since the light MPCM particles had the highest enhancement of heat transfer, this MPCM is examined for a range of flow regimes and particle concentrations, where the heat transfer coefficient is examined at the bottom wall of the channel. A crucial part of this analysis focuses on studying the impact of the volume fraction φ on the heat transfer by means of calculating the Nusselt number. Firstly, the local Nusselt number variation in the entrance region of the channel with respect to the Peclet number ($\mathrm{Pe} = \mathrm{Re}_{Dh}\mathrm{Pr}$) is demonstrated in Fig. 25. Throughout the length of the channel, the increase of microparticle volume fraction causes the thermal transfer to gradually increase. However, because in the developing region the heat transfer coefficient is significantly high, the impact of the particles on the heat transfer enhancement is negligible. In addition, the increase in the Peclet number, which by definition indicates a rise in advective fluid transport rather than diffusive transport, delays the development of the thermal boundary layer throughout the channel.

At the low value of $\mathrm{Pe} = 325$, the increase of the volume fraction from 0.1 to 0.2% slightly enhances thermal dissipation for the positions beyond the normalized location of $x/D_h = 2.5$. On the other hand, the incorporation of MPCM particles to a volume fraction of 0.4% leads to a sudden growth from the usual trend at $x/D_h = 1.25$. The point of bifurcation in trend is also noticed at $\mathrm{Pe} = 650$, 1300, and 2600 but delayed at the normalized locations of $x/D_h = 2.5$, 5, and 8, respectively. These points of bifurcation reveal that the influence of microparticles on thermal enhancement is only noticeable beyond such a location, and this location varies along the Peclet number. Similar behavior is exhibited in the research conducted by Ma *et al.* [74].

Turning attention to the region where heat transfer enhancement by MPCM particles is evident within the final regions of the entrance length, the volume fraction of $\varphi = 0.8\%$ led to a substantial increase in Nu_x for all Pe. This substantial enhancement of heat transfer is quantified with values of 10.77, 10.49, 7.55, and 6.19% compared with the base fluid for Pe values of 325, 650, 1300, and 2600, respectively. Conversely, the smallest MPCM concentration of $\varphi = 0.1\%$ had a slight increase in the heat transfer coefficient at $\mathrm{Pe} = 325$ and an insignificant impact on the thermal enhancement for $\mathrm{Pe} = 650$, 1300, and 2600. These findings reveal a positive correlation between the volume fraction and thermal enhancement in the entrance length of the channel.

In contrast to the previous figure, Figs. 26(a)–26(d) demonstrates the enhancement of the MPCM concentration in the fully developed region of the minichannel for various volume fractions at different flow regimes. In Fig. 26(a), it is apparent that the introduction of MCPM particles on the base fluids provides notable advancement in thermal performance. For higher Reynolds numbers of 100 and 200 [Figs. 26(b) and 26(c)], the effect of increasing the concentration of MPCMs starts to get more distinct.

Since the number of MPCM particles at a low volume fraction (0.1%) is few, increasing Re_{Dh} leads to the delay of the thermally developing region which will include more MPCM particles in that region and less at the thermally developed region. Consequently, the effect of $\varphi = 0.1\%$ on the heat transfer coefficient decreases when Re_{Dh} gradually increases from 50 to 300. A similar trend is observed with a volume fraction of 0.2% when raising the Reynolds number from 50 to 100 and then to 200, in contrast to $\mathrm{Re}_{Dh} = 300$, where the impact of MPCM particles on enhancing heat transfer becomes evident. This difference arises because, at $\mathrm{Re}_{Dh} = 300$, the MPCM particles possess sufficient momentum to migrate to the fully developed region where the MPCM particle influence on thermal enhancement becomes more apparent. In comparison with the base fluid, the incorporation of a volume fraction of 0.4% enhanced the heat transfer coefficient by $> 20\%$ for $\mathrm{Re}_{Dh} = 200$ and 21% for $\mathrm{Re}_{Dh} = 200$ at the end region ($x/D_h = 20$) of the channel. Notably, the highest volume fraction of 0.8% resulted in the greatest increase in Nu_x, where the recorded value remained consistently > 10 within the developed region for all flow regimes at various locations of the channel. The primary insight obtained from this part underscores that the heat transfer coefficients are affected not only by the volume fraction of particles but also by their distribution throughout the channel. Furthermore, it is noteworthy that, in the developed region exclusively, the increase of Reynolds numbers for higher volume fractions contributes to an improvement in thermal performance, whereas increasing the Reynolds number for lower volume fractions leads to a reduction in heat transfer.

It is essential to establish a comprehensive metric that quantifies the overall heat transfer coefficient as a singular parameter to fully encapsulate the extent of heat transfer enhancement when employing MPCM particles. A suitable way to represent this enhancement is by determining the average

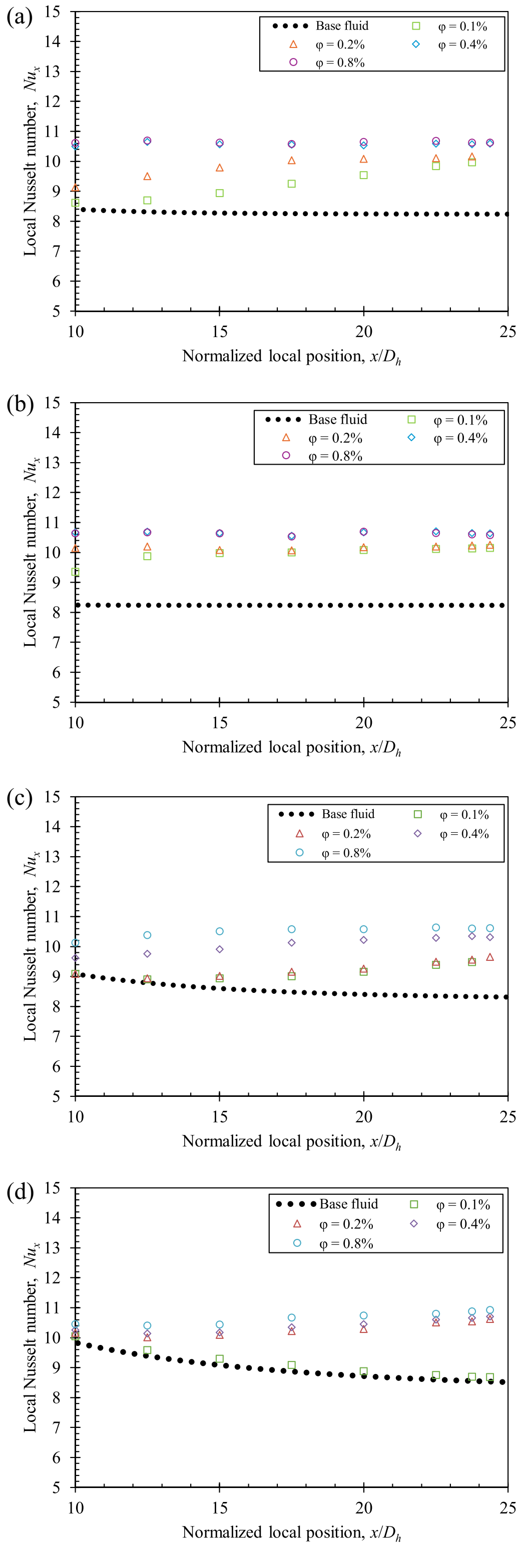

FIG. 26. A compilation of local Nusselt number trends is presented at the fully developed region, portraying the relationship with nondimensional local position across various flow regimes (a) Re = 50, (b) Re = 100, (c) Re = 200, and (d) Re = 300.

Nusselt number ($\overline{\text{Nu}}$) along the length of the channel surface

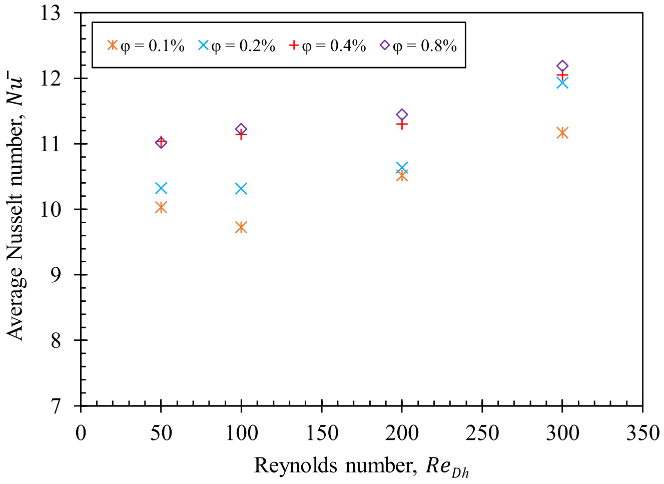

FIG. 27. Comparison between the average Nusselt number and Reynolds number for different volume fractions.

by the following correlation:

$$\overline{\text{Nu}} = \frac{1}{L}\int_0^L \text{Nu}_x \, dx\,. \tag{53}$$

By implementing the above equation, Fig. 27 is constructed. The average Nusselt number exhibits a decline as Re_{Dh} progresses from 50 to 100 for volume fractions of 0.1 and 0.2% due to reasons previously mentioned. Nevertheless, by increasing Re_{Dh} to 200 and 300, the decaying $\overline{\text{Nu}}$ trend for $\varphi = 0.1$ and 0.2% undergoes a transformation to an ascending trend due to the extended entrance length of the thermally developed region. Such a growth is the lowest when transitioning to an elevated flow regime, as shown in Table IV. However, when compared with the base fluid, the enhancement of the heat transfer coefficient is significantly improved. Furthermore, a linear growth pattern is exhibited when increasing the flow velocity from $\text{Re}_{Dh} = 200$ to the highest flow regime of $\text{Re}_{Dh} = 300$. Throughout different flow regimes, the most enhancing volume concentration is 0.8%, as demonstrated in Table IV. The core emphasis of this investigation reveals an enhancement in the overall heat transfer coefficient by increasing the Reynolds number and volume fraction. Nonetheless, the objective of continually elevating the Reynolds number to enhance thermal performance entails the tradeoff of increased pumping power. Consequently, the subsequent section discusses such a subject.

TABLE IV. The average enhancement percentage in comparison with the base fluid, for different volume fractions across various flow regimes.

φ/Re_{Dh}	50	100	200	300
0.1	21.31	17.61	27.18	35.13
0.2	24.89	24.73	28.65	44.29
0.4	33.49	34.73	36.65	45.77
0.8	33.21	35.76	38.49	47.39

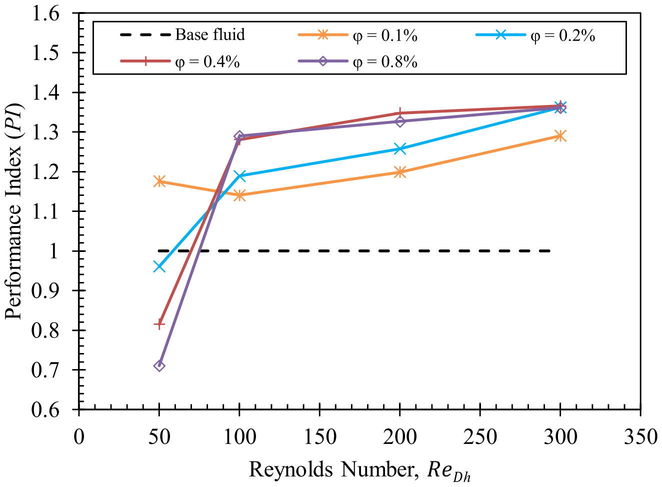

FIG. 28. An examination of the relationship between the performance index and Reynolds number is conducted across various volume fractions and base fluid configurations.

E. PI

The primary aim behind the integration of MPCMs into a minichannel is to attain optimal heat transfer conditions. This objective is realized through the pursuit of increased thermal enhancement while simultaneously minimizing pumping costs. To facilitate this pursuit, a correlation has been established to interrelate the friction factor with the average Nusselt number. The parameter employed is the PI or thermal enhancement factor defined as [75]

$$\mathrm{PI} = \left(\frac{\overline{\overline{\mathrm{Nu}}}}{\overline{\overline{\mathrm{Nu}}}_{\mathrm{bf}}}\right) \Big/ \left(\frac{f_D}{f_{D,\mathrm{bf}}}\right)^{1/3}. \tag{54}$$

Here, the subscript bf denotes the base fluid, where particles are absent for the average Nusselt number and friction factor. The friction factor f_D is obtained using [76]

$$f_D = 2\frac{\Delta p D_h}{\rho_f L \mathbf{u}_{\mathbf{m}}^2}. \tag{55}$$

Using Eq. (54), Fig. 28 is plotted. As expected, the PI for the volume fractions $\varphi = 0.2,\ 0.4,$ and 0.8% at a Reynolds number = 50 is below the value of unity. Such a value indicates the impracticability of incorporating MPCMs into the channel with such a flow regime due to the substantial escalation in pressure loss, which is not counterbalanced by a concurrent improvement in the heat transfer coefficient. On the other hand, the PI exceeds the value of 1 for $\mathrm{Re}_{Dh} > 100$ for all volume fractions. Upon increasing the Reynolds number to 200, a further augmentation in the PI is evident, as shown in Table V. The investigation of the PI within the specified range of volume fractions, excluding the flow regime at 50, has unveiled an ascending trend in the PI as the volume fraction escalates from 0.1 to 0.8% with increasing Reynolds number. Notably, the highest PI in this analysis is achieved at $\mathrm{Re}_{Dh} = 300$ for a volume fraction of 0.2, 0.4, and 0.8% with a PI of 1.36.

TABLE V. Quantitative analysis of the PI across various flow regimes at different volume fractions.

φ/Re_{Dh}	50	100	200	300
0.1	1.18	1.14	1.20	1.29
0.2	0.96	1.19	1.26	1.36
0.4	0.81	1.28	1.35	1.36
0.8	0.71	1.29	1.33	1.36

V. CONCLUSIONS

In conclusion, the presented hybrid numerical scheme integrates LBM with FDM, offering a promising approach for simulating the flow of MPCM particles. The numerical model specifically investigates the MPCM behavior near the heating channel surfaces. The comprehensive exploration of such behavior explored additional insights. These findings are briefly summarized as follows:

(1) Concentrating MPCM particles near the heating surfaces proves advantageous, resulting in lower surface temperatures and improved overall thermal performance.

(2) Both heavy and light MPCM particles exhibit a similar trend in reducing surface temperature, yet the light variant outperforms the heavy one in the amount of temperature reduction.

(3) Integrating more particles increased interparticle collisions, allowing particles to move toward higher-temperature regions, thereby enhancing thermal behavior at the cost of more pumping power.

(4) In the fully developed region, the heat transfer coefficients are influenced by both particle volume fraction and their distribution throughout the channel, but that is not the case for the entrance region.

It is noteworthy that, while an increase in φ enhances the heat transfer coefficient, it concurrently raises the resistance to particle flow, leading to an amplified pressure loss. Therefore, achieving an optimal condition becomes imperative. Within the scope of this analysis, it has been determined that this condition is attained at $\mathrm{Re}_{Dh} = 300$, when φ is set at 0.2, 0.4, and 0.8%, resulting in a maximum PI of 1.36.

ACKNOWLEDGMENT

Our sincere gratitude extends to ASPIRE for their generous funding (Grant No. AARE20-358), pivotal in realizing our research objectives.

---

[1] Z. Zhang, X. Wang, and Y. Yan, A review of the state-of-the-art in electronic cooling, e-Prime Adv. Electr. Eng. Electron. Energy **1**, 100009 (2021).

[2] H. M. Ali, Applications of combined/hybrid use of heat pipe and phase change materials in energy storage and cooling systems: A recent review, J. Energy Storage **26**, 100986 (2019).

[3] Z. He, Y. Yan, and Z. Zhang, Thermal management and temperature uniformity enhancement of electronic devices by micro heat sinks: A review, Energy **216**, 119223 (2021).

[4] L. Zhang, K. E. Goodson, and T. W. Kenny, *Silicon Microchannel Heat Sinks: Theories and Phenomena* (Springer, Berlin, 2004).

[5] E. G. Colgan, B. Furman, M. Gaynes, W. S. Graham, N. C. LaBianca, J. H. Magerlein, R. J. Polastre, M. B. Rothwell, R. J. Bezama, R. Choudhary *et al.*, A practical implementation of silicon microchannel coolers for high power chips, IEEE Trans. Compon. Packag. Technol. **30**, 218 (2007).

[6] S. Baraty Beni, A. Bahrami, and M. R. Salimpour, Design of novel geometries for microchannel heat sinks used for cooling diode lasers, Int. J. Heat Mass Transf. **112**, 689 (2017).

[7] T. Dang, J. T. Teng, and J. C. Chu, A study on the simulation and experiment of a microchannel counter-flow heat exchanger, Appl. Therm. Eng. **30**, 2163 (2010).

[8] K. Derakhshanpour, R. Kamali, and M. Eslami, Effect of rib shape and fillet radius on thermal-hydrodynamic performance of microchannel heat sinks: A CFD study, Int. Commun. Heat Mass Transfer **119**, 104928 (2020).

[9] S. A. Albdour, Z. Haddad, O. Z. Sharaf, A. Alazzam, and E. Abu-Nada, Micro/nano-encapsulated phase-change materials (ePCMs) for solar photothermal absorption and storage: Fundamentals, recent advances, and future directions, Prog. Energy Combust. Sci. **93**, 101037 (2022).

[10] L. Yang, J.-n. Huang, and F. Zhou, Thermophysical properties and applications of nano-enhanced PCMs: An update review, Energy Convers. Manag. **214**, 112876 (2020).

[11] L. Liu, G. Alva, Y. Jia, X. Huang, and G. Fang, Dynamic thermal characteristics analysis of microencapsulated phase change suspensions flowing through rectangular mini-channels for thermal energy storage, Energy Build. **134**, 37 (2017).

[12] A. MS and K. Venkatasubbaiah, Numerical investigation on laminar forced convection of MEPCM-water slurry flow through a micro-channel using Eulerian-Eulerian two-phase model, Therm. Sci. Eng. Prog. **22**, 100803 (2021).

[13] O. Z. Sharaf, A. N. Al-Khateeb, D. C. Kyritsis, and E. Abu-Nada, Four-way coupling of particle-wall and colloidal particle-particle interactions in direct absorption solar collectors, Energy Convers. Manag. **195**, 7 (2019).

[14] G. Zsembinszki, M. De Simone, M. Shirbani, M. Siavashi, and M. Bidabadi, Phase change materials energy storage enhancement schemes and implementing the lattice Boltzmann method for simulations: A review, Energies **16**, 1059 (2023).

[15] U. D'Ortona, D. Salin, M. Cieplak, R. B. Rybka, and J. R. Banavar, Two-color nonlinear Boltzmann cellular automata: Surface tension and wetting, Phys. Rev. E **51**, 3718 (1995).

[16] M. R. Swift, E. Orlandini, W. R. Osborn, and J. M. Yeomans, Lattice Boltzmann simulations of liquid-gas and binary fluid systems, Phys. Rev. E **54**, 5041 (1996).

[17] R. S. Qin, Mesoscopic interparticle potentials in the lattice Boltzmann equation for multiphase fluids, Phys. Rev. E **73**, 066703 (2006).

[18] Y. Gan, A. Xu, G. Zhang, and S. Succi, Discrete Boltzmann modeling of multiphase flows: Hydrodynamic and thermodynamic non-equilibrium effects, Soft Matter **11**, 5336 (2015).

[19] A. Xu, D. Zhang, and Y. Gan, Advances in the kinetics of heat and mass transfer in near-continuous complex flows, Front. Phys. **19**, 42500 (2024).

[20] C. Lin and K. H. Luo, Mesoscopic simulation of nonequilibrium detonation with discrete Boltzmann method, Combust. Flame **198**, 356 (2018).

[21] H. Li, A. Xu, G. Zhang, and Y. Shan, Rayleigh-Taylor instability under multi-mode perturbation: Discrete Boltzmann modeling with tracers, Commun. Theor. Phys. **74**, 115601 (2022).

[22] G. Zhang, A. Xu, D. Zhang, Y. Li, H. Lai, and X. Hu, Delineation of the flow and mixing induced by Rayleigh-Taylor instability through tracers, Phys. Fluids **33**, 07610 (2021).

[23] D. Zhang, A. Xu, J. Song, Y. Gan, Y. Zhang, and Y. Li, Specific-heat ratio effects on the interaction between shock wave and heavy-cylindrical bubble: Based on discrete Boltzmann method, Comput. Fluids **265**, 106021 (2023).

[24] C. S. Peskin, Flow patterns around heart valves: A numerical method, J. Comput. Phys. **10**, 252 (1972).

[25] M. A. A. Spaid and F. R. Phelan, Lattice Boltzmann methods for modeling microscale flow in fibrous porous media, Phys. Fluids **9**, 2468 (1997).

[26] M. J. Krause, F. Klemens, T. Henn, R. Trunk, and H. Nirschl, Particle flow simulations with homogenised lattice Boltzmann methods, Particuology **34**, 1 (2017).

[27] A. Kummerländer, S. Avis, H. Kusumaatmaja, F. Bukreev, M. Crocoll, D. Dapelo, N. Hafen, S. Ito, J. Jeßberger, J. E. Marquardt, J. Mödl, T. Pertzel, F. Prinz, F. Raichle, M. Schecher, S. Simonis, D. Teutscher, and M. J. Krause, OpenLB Release 1.6: Open Source Lattice Boltzmann Code, Version 1.6. Apr. (2023), doi: 10.5281/zenodo.7773497.

[28] A. Gupta, M. Sbragaglia, and A. Scagliarini, Hybrid lattice Boltzmann/finite difference simulations of viscoelastic multicomponent flows in confined geometries, J. Comput. Phys. **291**, 177 (2015).

[29] S. A. Hosseini, H. Safari, N. Darabiha, D. Thévenin, and M. Krafczyk, Hybrid lattice Boltzmann-finite difference model for low mach number combustion simulation, Combust. Flame **209**, 394 (2019).

[30] D. E. Beasley, C. Ramanarayanan, and H. Torab, Thermal response of a packed bed of spheres containing a phase-change material, Int. J. Energy Res. **13**, 253 (1989).

[31] A. A. Mohamad, *Lattice Boltzmann Method: Fundamentals and Engineering Applications with Computer Codes* (Springer, London, 2019).

[32] P. L. Bhatnagar, E. P. Gross, and M. Krook, A model for collision processes in gases. I. Small amplitude processes in charged and neutral one-component systems, Phys. Rev. **94**, 511 (1954).

[33] T. Krüger, H. Kusumaatmaja, A. Kuzmin, O. Shardt, G. Silva, and E. M. Viggen, *The Lattice Boltzmann Method: Principles and Practice* (Springer, Cham, 2017).

[34] R. Trunk, T. Weckerle, N. Hafen, G. Thäter, H. Nirschl, and M. J. Krause, Revisiting the homogenized lattice Boltzmann method with applications on particulate flows, Computation **9**, 11 (2021).

[35] X. Shan and H. Chen, Lattice Boltzmann model for simulating flows with multiple phases and components, Phys. Rev. E **47**, 1815 (1993).

[36] Z. Guo, C. Zheng, and B. Shi, Discrete lattice effects on the forcing term in the lattice Boltzmann method, Phys. Rev. E **65**, 046308 (2002).

[37] A. L. Kupershtokh, D. A. Medvedev, and D. I. Karpov, On equations of state in a lattice Boltzmann method, Comput. Math. Appl. **58**, 965 (2009).

[38] R. Huang, H. Wu, and P. Cheng, A new lattice Boltzmann model for solid-liquid phase change, Int. J. Heat Mass Transf. **59**, 295 (2013).

[39] L. Li, R. Mei, and J. F. Klausner, Lattice Boltzmann models for the convection-diffusion equation: $D2Q5$ vs $D2Q9$, Int. J. Heat Mass Transf. **108**, 41 (2017).

[40] J. A. Bocanegra, A. Marchitto, and M. Misale, Study of a square single-phase natural circulation loop using the lattice Boltzmann method, Appl. Mech. **4**, 927 (2023).

[41] H. B. Huang, X. Y. Lu, and M. C. Sukop, Numerical study of lattice Boltzmann methods for a convection-diffusion equation coupled with Navier-Stokes equations, J. Phys. A **44**, 055001 (2011).

[42] S. Tao, A. Xu, Q. He, B. Chen, and F. G. F. Qin, A curved lattice Boltzmann boundary scheme for thermal convective flows with Neumann boundary condition, Int. J. Heat Mass Transf. **150**, 119345 (2020).

[43] O. Z. Sharaf, A. N. Al-Khateeb, D. C. Kyritsis, and E. Abu-Nada, Direct absorption solar collector (DASC) modeling and simulation using a novel Eulerian-Lagrangian hybrid approach: Optical, thermal, and hydrodynamic interactions, Appl. Energy **231**, 1132 (2018).

[44] Y. Addad, M. Abutayeh, and E. Abu-Nada, Effects of nanofluids on the performance of a PCM-based thermal energy storage system, J. Energy Eng. **143**, 04017006 (2017).

[45] W. R. Marshall and W. E. Ranz, Evaporation from drops—Part I, Chem. Eng. Prog. **48**, 141 (1952).

[46] *Multiphase Flow Handbook*, edited by E. Michaelides, C. T. Crowe, and J. D. Schwarzkopf (CRC Press, Boca Raton, 2016).

[47] J. Tu, K. Inthavong, and G. Ahmadi, *Computational Fluid and Particle Dynamics in the Human Respiratory System* (Springer, Dordrecht, 2013).

[48] L. Xu, L. Pu, S. Zhang, and Z. Ma, Thermo-fluidic performance of microencapsulated phase change material slurry in thermal energy storage, J. Energy Storage **43**, 103247 (2021).

[49] S. Laín, M. Sommerfeld, and J. Kussin, Experimental studies and modelling of four-way coupling in particle-laden horizontal channel flow, Int. J. Heat Fluid Flow **23**, 647 (2002).

[50] S. Laín and J. A. García, Study of four-way coupling on turbulent particle-laden jet flows, Chem. Eng. Sci. **61**, 6775 (2006).

[51] S. K. Friedlander, *Smoke, Dust and Haze: Fundamentals of Aerosol Behaviour* (Wiley, New York, 1977).

[52] C. T. Crowe, J. D. Schwarzkopf, M. Sommerfeld, and Y. Tsuji, *Multiphase Flows with Droplets and Particles*, 2nd ed. (Taylor & Francis Group, LLC, Boca Raton, 2012).

[53] B. Nassauer and M. Kuna, Contact forces of polyhedral particles in discrete element method, Granul. Matter **15**, 349 (2013).

[54] C. G. Ilea, P. Kosinski, and A. C. Hoffmann, The effect of polydispersity on dust lifting behind shock waves, Powder Technol. **196**, 194 (2009).

[55] A. Safdari and K. C. Kim, Lattice Boltzmann simulation of solid particles behavior in a three-dimensional lid-driven cavity flow, Comput. Math. Appl. **68**, 606 (2014).

[56] A. ten Cate, C. H. Nieuwstad, J. J. Derksen, and H. E. A. Van den Akker, Particle imaging velocimetry experiments and lattice-Boltzmann simulations on a single sphere settling under gravity, Phys. Fluids **14**, 4012 (2002).

[57] Y. Chen, Q. Cai, Z. Xia, M. Wang, and S. Chen, Momentum-exchange method in lattice Boltzmann simulations of particle-fluid interactions, Phys. Rev. E **88**, 013303 (2013).

[58] Z. Xia, K. W. Connington, S. Rapaka, P. Yue, J. J. Feng, and S. Chen, Flow patterns in the sedimentation of an elliptical particle, J. Fluid Mech. **625**, 249 (2009).

[59] L. Wang, Z. L. Guo, and J. C. Mi, Drafting, kissing and tumbling process of two particles with different sizes, Comput. Fluids **96**, 20 (2014).

[60] D. Nie and J. Lin, A LB-DF/FD method for particle suspensions, Commun. Comput. Phys. **7**, 544 (2010).

[61] Z. G. Feng and E. E. Michaelides, The immersed boundary-lattice Boltzmann method for solving fluid-particles interaction problems, J. Comput. Phys. **195**, 602 (2004).

[62] H. Zhang, Y. Tan, S. Shu, X. Niu, F. X. Trias, D. Yang, H. Li, and Y. Sheng, Numerical investigation on the role of discrete element method in combined LBM-IBM-DEM modeling, Comput. Fluids **94**, 37 (2014).

[63] T. Hagemeier, D. Thévenin, and T. Richter, Settling of spherical particles in the transitional regime, Int. J. Multiphase Flow **138**, 103589 (2021).

[64] H. Von Wahl, T. Richter, S. Frei, and T. Hagemeier, Falling balls in a viscous fluid with contact: Comparing numerical simulations with experimental data, Phys. Fluids **33**, 033304 (2021).

[65] E. Burman, M. A. Fernández, S. Frei, and F. M. Gerosa, A mechanically consistent model for fluid–structure interactions with contact including seepage, Comp. Meth. Appl. Mech. Eng. **392**, 114637 (2022).

[66] J. E. Marquardt, U. J. Römer, H. Nirschl, and M. J. Krause, A discrete contact model for complex arbitrary-shaped convex geometries, Particuology **80**, 180 (2023).

[67] T. L. Bergman, A. S. Lavine, F. P. Incropera, and D. P. DeWitt, *Fundamentals of Heat and Mass Transfer*, 7th ed. (Wiley and Sons, Inc., Hoboken, 2011).

[68] *Heat Transfer Handbook*, edited by A. Bejan and A. L. Kraus (John Wiley & Sons, Inc., Hoboken, 2003).

[69] E. W. J. Mardles, Viscosity of suspensions and the Einstein equation, Nature (London) **145**, 970 (1940).

[70] H. C. Brinkman, The viscosity of concentrated suspensions and solutions, J. Chem. Phys. **20**, 571 (1952).

[71] F. F. Abraham, Functional dependence of drag ccoefficient of a sphere on Reynolds number, Phys. Fluids **13**, 2194 (1970).

[72] B. Chen, X. Wang, R. Zeng, Y. Zhang, X. Wang, J. Niu, Y. Li, and H. Di, An experimental study of convective heat transfer with microencapsulated phase change material suspension: Laminar flow in a circular tube under constant heat flux, Exp. Therm Fluid Sci. **32**, 1638 (2008).

[73] M. Chen, Y. Wang, and Z. Liu, Experimental study on microencapsulated phase change material slurry flowing in straight and wavy microchannels, Appl. Therm. Eng. **190**, 116841 (2021).

[74] H. Ma, B. He, L. Su, and D. He, Heat transfer enhancement of nanofluid flow at the entry region of microtubes, Int. J. Therm. Sci. **184**, 107944 (2023).

[75] M. M. Generous, E. Abu-Nada, and A. Alazzam, Exploring the potential of hybrid nanofluids for enhanced heat transfer in a duct: A comprehensive study utilizing a phases-interaction driven multiphase mixture model, Int. J. Thermofluids **20**, 100453 (2023).

[76] M. J. S. de Lemos, *Turbulence in Porous Media: Modeling and Applications*, 2nd ed. (Elsevier, London, 2012).